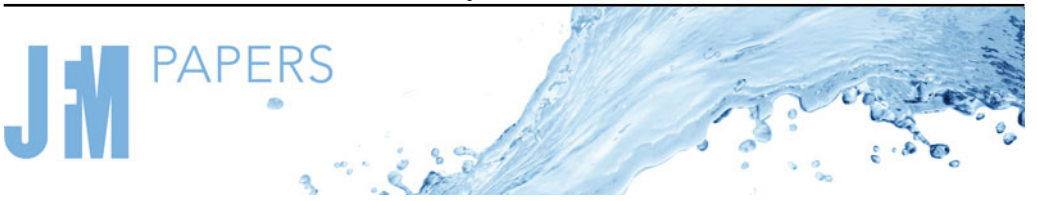
J. Fluid Mech. (2026), *vol.* 1029, A30, doi:10.1017/jfm.2026.11152



A unified variational framework and lattice Boltzmann method for non-isothermal two-phase flows with phase transitions and wetting effects

Zhonghua Qiao[1], **Xianmin Xu**[2], **Xuguang Yang**[3] **and Yuze Zhang**[4]

[1]Department of Applied Mathematics, The Hong Kong Polytechnic University, Hung Hom, Hong Kong

[2]State Key Laboratory of Mathematical Sciences, Academy of Mathematics and Systems Science, Chinese Academy of Sciences, Beijing 100190, PR China

[3]School of Mathematics and Statistics, Hunan First Normal University, Changsha, PR China

[4]School of Mathematical Sciences, Ministry of Education key Laboratory of NSLSCS, Nanjing Normal University, Nanjing, PR China

Corresponding authors: Xianmin Xu, xmxu@lsec.cc.ac.cn; Xuguang Yang, sfxuguang@hnfnu.edu.cn

(Received 25 June 2025; revised 28 November 2025; accepted 7 January 2026)

This study presents a novel extension of the Onsager variational principle to incorporate inertial and thermal effects in fluid dynamics, thereby establishing a unified variational framework for modelling non-isothermal two-phase flows with liquid–vapour phase transitions and wetting effects on solid substrates. From this framework, we naturally derive a thermodynamically consistent model for the fluid system, comprising two-phase Navier–Stokes equations, an equation for the total energy, and dynamic boundary conditions that account for thermal and wetting effects. The derivation is independent of the equation of state, and generalises the dynamic van der Waals theory. To address the computational complexity of the resulting dynamic system, we propose a lattice Boltzmann method based on double distribution functions, which enables accurate and robust simulations of coupled fluid and thermal transport. Numerical experiments – including droplet evaporation, bubble nucleation and departure, and Leidenfrost droplet impact – demonstrate good agreement with theoretical predictions and experimental data, indicating that the proposed numerical method can effectively capture complex thermohydrodynamic phenomena.

Key words: variational methods, multiphase flow

https://doi.org/10.1017/jfm.2026.11152 Published online by Cambridge University Press

© The Author(s), 2026. Published by Cambridge University Press.

1. Introduction

Non-isothermal multiphase flows involving phase transitions and wetting effects are ubiquitous in natural processes and diverse industrial applications, such as petrochemical industries, materials engineering and biomedical fields. These systems exhibit fascinating phenomena, including the Leidenfrost effect of droplets on hot substrates (Quéré 2013; Bouillant *et al.* 2018; Graeber *et al.* 2021), evaporation-induced droplet motion (Cira, Benusiglio & Prakash 2015; Man & Doi 2017; Kavuri *et al.* 2025), and directional fluid transport with enhanced heat transfer (in Cassie–Baxter states) on hydrophobic surfaces (Hodes *et al.* 2023; Mayer *et al.* 2025). Accurate and efficient numerical modelling strategies are therefore crucial for predicting the complex behaviours of such systems, significantly advancing our understanding of their underlying physical mechanisms.

Extensive research efforts have been devoted to elucidating the dynamics of liquid–vapour phase transitions (Hohenberg & Halperin 1977; Onuki 2002) and associated flow and heat transfer characteristics (among many others, see e.g. Dhir 1998; Cheng *et al.* 2014; Zhakhovsky *et al.* 2019; Wilson & D'Ambrosio 2023; Tang *et al.* 2024). Physically, these phase transitions represent inherently multiscale processes spanning microscopic to macroscopic length scales, where interfacial thermohydrodynamics plays a crucial and often dominant role (Zhakhovsky *et al.* 2019). Incorporating wetting effects necessitates addressing the moving contact line problem – another inherently multiscale phenomenon that presents substantial modelling challenges (see Huh & Scriven 1971; Jacqmin 2000; Qian, Wang & Sheng 2003; Ren 2007; Shikhmurzaev 2007; Snoeijer & Andreotti 2013; Guan *et al.* 2016; Zhang & Xu 2022; and references therein). Consequently, accurate modelling and quantitative simulation of non-isothermal two-phase flows involving both phase transitions and wetting effects pose significantly greater computational and theoretical difficulties.

Among various approaches, the dynamic van der Waals theory establishes a theoretical model for one-component two-phase hydrodynamic flows involving liquid–vapour transitions under non-isothermal conditions (Onuki 2005, 2007). To incorporate wetting effects, Liu, Qian & Xu (2012) developed appropriate boundary conditions through an extension of Waldmann's method (Waldmann 1967). These formulations have subsequently been applied to simulate thermal-gradient-driven droplet motion (Xu & Qian 2012), boiling phenomena (Xu & Qian 2014) and the Leidenfrost effect (Xu & Qian 2013). While effective for simple fluids through the van der Waals equation of state, these models face limitations due to the theoretical complexity inherent in deriving both dynamic equations and boundary conditions within this framework. Consequently, the approach has not been generalised to fluid systems with more complex molecular interactions, such as those governed by the Peng–Robinson equation of state (Peng & Robinson 1976) – despite its extensive industrial applications in petrochemical contexts (Lopez-Echeverry, Reif-Acherman & Araujo-Lopez 2017; Kou & Sun 2018*b*).

Numerous computational methods have been developed for simulating non-isothermal two-phase flows with phase transitions, each employing distinct theoretical frameworks and numerical implementations. Prominent approaches include: the volume-of-fluid method (Welch & Wilson 2000), valued for sharp interface capture; the level-set technique (Tomar *et al.* 2005), noted for smooth interface tracking; diffuse interface methods where interfaces are implicitly represented through density functions (single-component systems) or phase-field functions (multi-component systems) (Anderson, McFadden & Wheeler 1998; Guo & Lin 2015; Schweigler *et al.* 2017); and mesoscopic methods (Gong & Cheng 2012; Li, Luo & Kang 2016; Huang, Wu & Adams 2021; Wang, Huang & He 2022*b*), prized for intrinsic parallelism and microscopic interaction modelling. Numerical simulations for moving contact line problems also attract much

https://doi.org/10.1017/jfm.2026.11152 Published online by Cambridge University Press

attentions (e.g. Sui, Ding & Spelt 2014; Xu 2023). Nevertheless, quantitative simulation of non-isothermal two-phase flows incorporating both phase transitions and wetting effects remains particularly challenging.

The Onsager variational principle (Onsager 1931*b*) provides a powerful framework for deriving both complete and reduced models in soft matter systems (Doi 2011, 2013; Man & Doi 2017; Xu, Di & M 2016). It has been specifically applied to derive generalised Navier slip boundary conditions for phase-field models of moving contact lines (Qian, Wang & Sheng 2006) and macroscopic boundary conditions for sharp-interface models (Zhang & Xu 2022). In such applications, however, inertial effects are neglected as the original formulation of the Onsager principle applies exclusively to overdamped systems. This limitation has motivated the development of alternative theoretical frameworks, including the GENERIC approach (Öttinger 2005), the energetic variational approach (Hyon, Kwak & Liu 2010; Wang & Liu 2022), and generalised Onsager principles (Wang 2021). Notably, these extensions typically abandon the variational structure of the original principle – namely, the minimisation of a Rayleigh function with respect to fluxes. In addition, as far as we know, the principle has not been applied to non-isothermal two-phase flow problems with phase transition and inertial effects.

This work develops a unified variational framework and an efficient numerical method for non-isothermal two-phase flows involving liquid–vapour phase transitions and wetting effects. The Onsager variational principle is extended for modelling non-isothermal systems with inertial effects through a novel approach. This approach incorporates the mass, momentum and energy conservation equations as constraints to optimise a Rayleigh functional associated with entropy production. The resulting variational problem directly leads to a system of equations that describe non-isothermal flows with phase transitions and wetting effects. Rooted in the Onsager variational principle, the derivation explicitly demonstrates that the system satisfies both the Onsager reciprocal relations and the second law of thermodynamics, while inherently conserving mass, momentum and energy. Notably, the derivation remains independent of the choice of equation of state. By adopting the van der Waals model for internal energy and entropy, the dynamic van der Waals theory models with hydrodynamic boundary conditions (Onuki 2007; Liu *et al.* 2012) are recovered through a derivation that is significantly simpler than in previous approaches. The framework readily accommodates alternative equations of state, such as the Peng–Robinson model, thereby yielding a dynamic Peng–Robinson formulation. Moreover, the derivation can be straightforwardly generalised to multicomponent systems (e.g. Kou & Sun 2018*a*) to incorporate phase transitions and wetting effects.

To efficiently solve the non-isothermal multiphase dynamic equations, a lattice Boltzmann method (LBM) is developed. As a mesoscopic numerical framework, the LBM is widely recognised as a computationally robust and efficient technique for simulating complex fluid problems (Chen & Doolen 1998; Aidun & Clausen 2010; Guo & Shu 2013; Huang, Sukop & Lu 2015; Qiao, Yang & Zhang 2024; Zhang *et al.* 2025). Unlike conventional computational fluid dynamics approaches that directly solve macroscopic equations, the LBM employs kinetic theory to describe fluid dynamics at the mesoscopic level. The discretisation scheme utilises two distribution functions: one for the mass and momentum equations, and another for the energy equation. This kinetic approach offers significant advantages, including algorithmic simplicity, straightforward boundary condition implementation, and intrinsic parallelisability (He, Liu & Li 2019; Qiao, Yang & Zhang 2019, 2021). The proposed model and numerical method are validated through simulations of key phenomena, such as droplet evaporation and dynamics wetting on heated surface, showing excellent agreement with experimental observations. In addition, we simulate bubble nucleation during boiling, which is induced by spinodal

https://doi.org/10.1017/jfm.2026.11152 Published online by Cambridge University Press

instability in our model. The onset temperature is higher than the experimental value. Nevertheless, the departure diameter of the droplet and the dynamic behaviour are consistent with experimental observations. To simulate the genuine nucleation with correct onset temperature, a mesoscopic model with stochastic forces should be used, as in Gallo *et al.* (2020, 2021, 2023).

The remainder of this paper is organised as follows. Section 2 presents a generalisation of the Onsager principle to incorporate inertial and non-isothermal effects for one-component two-phase flows with moving contact lines. Section 3 introduces the discrete velocity kinetic model employing a double distribution function framework and the corresponding lattice Boltzmann numerical implementation. Numerical validations and discussions, employing the van der Waals equation of state for simplicity, are presented in § 4. Finally, § 5 provides a brief summary and some concluding remarks.

2. A variational framework to the non-isothermal two-phase flows

The Onsager variational principle is a fundamental law in thermodynamics. Originally proposed by Lars Onsager (1931*a*,*b*), it has been extensively applied to derive models for various overdamped systems (Doi 2011, 2013). In particular, one can derive a Cahn–Hilliard–Stokes system with moving contact lines in a simple way by minimising the Rayleigh function (Qian *et al.* 2006). This section extends the variational principle to the non-isothermal system with inertial and thermo-wetting effects.

2.1. *Basic conservation equations*

Consider a one-component two-phase system occupied in a domain $\Omega \in \mathbb{R}^d$, $d = 2, 3$. We have three basic physical quantities to describe the dynamics of the systems, which are the number density $n(\boldsymbol{x}, t)$, the internal energy density $e(\boldsymbol{x}, t)$ and the velocity $\boldsymbol{u}(\boldsymbol{x}, t)$. They are functions of space $\boldsymbol{x} \in \Omega$ and time t. When there is a two-phase interface, the gradient contribution of n to the energy should be considered (Onuki 2007). This leads to a modified internal energy density function

$$\hat{e}(\boldsymbol{x}, t) = e(\boldsymbol{x}, t) + \frac{K}{2}|\nabla n|^2, \tag{2.1}$$

where K is a positive parameter. By further considering the kinetic energy, the total energy density is given by

$$\hat{e}_{tot}(\boldsymbol{x}, t) = \hat{e}(\boldsymbol{x}, t) + \frac{m_0 n}{2}\boldsymbol{u}^2, \tag{2.2}$$

where m_0 is the mass of one molecule. Thus $m_0 n$ defines a density of the fluids, denoted as $\rho(x, t)$ for later use.

The general conservation equations for the number density n, momentum density $m_0 n\boldsymbol{u}$ and total energy density e_{tot} are given by

$$\frac{\partial n}{\partial t} + \nabla \cdot (n\boldsymbol{u}) = 0, \tag{2.3}$$

$$m_0\left(\frac{\partial n\boldsymbol{u}}{\partial t} + \nabla \cdot (n\boldsymbol{u}\boldsymbol{u})\right) = \nabla \cdot \hat{\boldsymbol{\sigma}}, \tag{2.4}$$

$$\frac{\partial e_{tot}}{\partial t} + \nabla \cdot (e_{tot}\boldsymbol{u}) = \nabla \cdot (\hat{\boldsymbol{\sigma}}\boldsymbol{u}) - \nabla \cdot \boldsymbol{j}_e, \tag{2.5}$$

where $\boldsymbol{j}_e$ is the heat flux, and $\hat{\boldsymbol{\sigma}}$ is the stress tensor. These three equations correspond to the laws of mass, momentum and energy conservation in classical mechanics. The system is not closed, as $\boldsymbol{j}_e$ and $\hat{\boldsymbol{\sigma}}$ are not yet known.

https://doi.org/10.1017/jfm.2026.11152 Published online by Cambridge University Press

In addition, we need to consider proper boundary conditions. For simplicity, we assume that $\Gamma_S = \partial\Omega$ is the solid–fluid interface. We also suppose that the inner energy densities on the solid boundary are functions of n given by $e_b(n)$ as in Onuki (2007). Then the energy conservation equation on the boundary is given by

$$\frac{\partial e_b}{\partial t} + \nabla_\Gamma \cdot (e_b \boldsymbol{u}) = \boldsymbol{j}_e \cdot \boldsymbol{\nu} - \boldsymbol{j}_{e,s} \cdot \boldsymbol{\nu}, \tag{2.6}$$

where $\boldsymbol{j}_{e,s} \cdot \boldsymbol{\nu}$ is the thermal flux from the boundary to solid phase, and $\boldsymbol{j}_e \cdot \boldsymbol{\nu}$ is the thermal flux from the liquid phase to the boundary. Here, $\boldsymbol{\nu}$ is the unit outward normal vector on Γ_S. The equation implies that the difference between two fluxes leads to the change of surface energy density e_b. More explanations on the equation can be found in Liu *et al.* (2012). Notice that e_b is a function of n. The above equation is reduced to

$$e_b'(n)\,\frac{\partial n}{\partial t} + \nabla_\Gamma \cdot (e_b \boldsymbol{u}) = \boldsymbol{j}_e \cdot \boldsymbol{\nu} - \boldsymbol{j}_{e,s} \cdot \boldsymbol{\nu}. \tag{2.7}$$

In addition, we also assume that $\boldsymbol{u} \cdot \boldsymbol{\nu} = 0$ on Γ_S, i.e. the boundary is impenetrable. However, the tangential velocity $\boldsymbol{u}_\tau = \boldsymbol{P}\boldsymbol{u} = \boldsymbol{u} - (\boldsymbol{u} \cdot \boldsymbol{\nu})\boldsymbol{\nu}$ may not be zero due to the slip effect. Here, we define the tangential projection operator $\boldsymbol{P} := \boldsymbol{I} - \boldsymbol{\nu}\boldsymbol{\nu}^{\mathrm{T}}$.

To close the system, the specific expressions for the stress tensor and heat flux, along with the necessary boundary conditions, must be determined. These will be derived in the following subsections using an extended Onsager variational principle.

2.2. *The entropy functional*

Before introducing the Onsager principle for non-isothermal systems, we first specify the entropy density $s(n, e)$ in the system, which is a function of the number density n and the internal energy density e. Standard thermodynamic theory defines the temperature $T(n, e)$, i.e.

$$\frac{1}{T} = \frac{\partial s(n, e)}{\partial e}. \tag{2.8}$$

For example, for the van der Waals fluids (see Onuki 2007), we have

$$s(n, e) = -k_B n\left(d \ln \hbar + \frac{d}{2} \ln \frac{d\pi k_B n}{m_0} - \frac{d}{2} \ln(e + \epsilon a^d n^2) + \ln \frac{n}{1 - a^d n}\right) + \frac{k_B n(d+2)}{2},$$
$$T(n, e) = \frac{2(e + \epsilon a^d n^2)}{d k_B n}, \tag{2.9}$$

where k_B is the Boltzmann constant, $\hbar$ is the Planck constant, a is the radius of a molecule, and ϵ is the magnitude of attracting potential. Notice that in the literature, it is common to take the number density n and the temperature T as primary unknowns, with the internal energy e and entropy density s being functions of n and T. A straightforward calculation then yields the formula used in our work. Other examples include the widely used Peng–Robinson equation of state. The expressions for the entropy s and internal energy e can be found in Smejkal & Miky (2017) and Kou & Sun (2018*b*).

Similar to the case for internal energy density, we must also incorporate a gradient contribution into the entropy density when a liquid–vapour interface is present. The modified entropy density is then given by (cf. Onuki 2007)

$$\hat{s}(n, e) = s(n, e) - \frac{C}{2}|\nabla n|^2, \tag{2.10}$$

https://doi.org/10.1017/jfm.2026.11152 Published online by Cambridge University Press

where C is a positive parameter. In addition, the entropy density on the solid boundary Γ_S is also a function of n, given by $s_b(n)$. Then the total entropy is calculated by

$$\mathcal{S} := \int_{\Omega} \hat{s}(n(\boldsymbol{x}, t), e(\boldsymbol{x}, t))\, \mathrm{d}x + \int_{\Gamma_S} s_b(n(\boldsymbol{x}, t))\, \mathrm{d}A, \tag{2.11}$$

which is a functional with respect to n and e.

2.3. *The extended Onsager principle for non-isothermal systems*

To use the Onsager principle for non-isothermal systems, we define a Rayleigh functional,

$$\mathcal{R}(\boldsymbol{u}, \boldsymbol{j}_e, \boldsymbol{u}_\tau|_{\Gamma_S}, \dot{n}|_{\Gamma_S}) := \Phi - \dot{\mathcal{S}}_{prod}, \tag{2.12}$$

where $\Phi(\boldsymbol{u}, \boldsymbol{j}_e, \boldsymbol{u}_\tau|_{\Gamma_S}, \dot{n}|_{\Gamma_S})$ is the entropy production function, and $\dot{\mathcal{S}}_{prod}$ is the time changing rate of the entropy produced in the system, which is the total entropy minus that from the environment (noticing that the system is not closed due to heat transfer on the solid boundary). The entropy production function of the system is given by

$$\begin{aligned}\Phi := &\int_{\Omega} \left(\frac{\eta}{T} \left\| \frac{\nabla \boldsymbol{u} + \nabla \boldsymbol{u}^{\mathrm{T}}}{2} - \frac{1}{d}(\nabla \cdot \boldsymbol{u})\boldsymbol{I} \right\|_F^2 + \frac{\xi}{2T}(\nabla \cdot \boldsymbol{u})^2 + \frac{1}{2\lambda} \left| \frac{\boldsymbol{j}_e}{T} \right|^2 \right) \mathrm{d}x \\ &+ \int_{\Gamma_S} \left(\frac{\alpha}{2T} |\boldsymbol{u}_\tau|^2 + \frac{\beta}{2T} \dot{n}^2 \right) \mathrm{d}A,\end{aligned} \tag{2.13}$$

where $\boldsymbol{I}$ is the unit matrix, $\|\cdot\|_F$ denotes the Frobenius norm, $\dot{n}$ is the material derivative of n, d is the spacial dimension, λ is thermal conductivity, α is the slip coefficient, β is the phenomenological relaxation parameter, and η and ξ are the shear and bulk viscosities, respectively. The entropy producing rate is given by

$$\dot{\mathcal{S}}_{prod} := \dot{\mathcal{S}} + \int_{\Gamma_S} \frac{\boldsymbol{j}_{e,s} \cdot \boldsymbol{\nu}}{T}\, \mathrm{d}A - \int_{\Gamma_S} \frac{1}{T} \boldsymbol{P}\hat{\boldsymbol{\sigma}}\boldsymbol{\nu} \cdot \boldsymbol{u}_\tau\, \mathrm{d}A, \tag{2.14}$$

which is the rate of increase of the total entropy in the bulk, plus outgoing entropy flux through the domain boundary, and minus the entropy production rate due to the work done at the boundary. Here, $\boldsymbol{\nu}$ is the outer normal direction on Γ_S. For adiabatic and no-slip boundary conditions, the last two terms vanish.

We propose an extended version of the Onsager principle as follows. The constitutive equations and the boundary conditions can be obtained by minimising the Rayleigh functional, i.e.

$$\min_{\boldsymbol{u}, \boldsymbol{j}_e, \boldsymbol{u}_\tau|_\Gamma, \dot{n}|_\Gamma} \mathcal{R} \quad \text{s.t.} \quad (2.3)\text{-}(2.7). \tag{2.15}$$

In the following, we derive in detail the expressions for $\hat{\boldsymbol{\sigma}}$ and $\boldsymbol{j}_e$, along with the boundary conditions characterising the wetting and thermal effects.

2.4. *Derivations of the constitutive relations and boundary conditions*

We first use (2.3)–(2.7) to express $\dot{\mathcal{S}}$ as a functional of $\boldsymbol{u}$, $\boldsymbol{j}_e$, $\boldsymbol{u}_\tau|_{\Gamma_S}$ and $\dot{n}|_{\Gamma_S}$. Direct calculations lead to

https://doi.org/10.1017/jfm.2026.11152 Published online by Cambridge University Press

$$\dot{\mathcal{S}} = \int_\Omega \left(\frac{\partial \hat{s}}{\partial t} + \nabla \cdot (\hat{s}\boldsymbol{u}) \right) \mathrm{d}x + \int_{\Gamma_s} \left(\frac{\partial s_b}{\partial t} + \nabla_\Gamma \cdot (s_b \boldsymbol{u}_\tau) \right) \mathrm{d}A = \int_\Omega \frac{\partial \hat{s}}{\partial t} \,\mathrm{d}x + \int_{\Gamma_s} \frac{\partial s_b}{\partial t} \,\mathrm{d}A$$
$$= \int_\Omega \left(\frac{\partial s}{\partial e}\frac{\partial e}{\partial t} + \frac{\partial s}{\partial n}\frac{\partial n}{\partial t} - \frac{1}{2}\frac{\partial}{\partial t}(C\,|\nabla n|^2) \right) \mathrm{d}x + \int_{\Gamma_s} s_b'(n)\,\frac{\partial n}{\partial t}\,\mathrm{d}A$$
$$= \int_\Omega \left(\frac{\partial s}{\partial e}\frac{\partial \hat{e}}{\partial t} - \frac{1}{2}\frac{\partial s}{\partial e}\frac{\partial}{\partial t}(K\,|\nabla n|^2) + \frac{\partial s}{\partial n}\frac{\partial n}{\partial t} - \frac{1}{2}\frac{\partial}{\partial t}(C\,|\nabla n|^2) \right) \mathrm{d}x + \int_{\Gamma_s} s_b'(n)\,\frac{\partial n}{\partial t}\,\mathrm{d}A$$
$$= \int_\Omega \left(\frac{1}{T}\frac{\partial \hat{e}}{\partial t} + \frac{\partial s}{\partial n}\frac{\partial n}{\partial t} - \frac{M(T)}{T}\,\nabla n \cdot \nabla \frac{\partial n}{\partial t} \right) \mathrm{d}x + \int_{\Gamma_s} s_b'(n)\,\frac{\partial n}{\partial t}\,\mathrm{d}A. \tag{2.16}$$

Here, we have used the definition of the temperature, i.e. $1/T = \partial s/\partial e$, and $M(T) := K + CT$.

Consider (2.5). The time derivative of total energy density e_{tot} can be evaluated as

$$\frac{\partial e_{tot}}{\partial t} = \frac{\partial \hat{e}}{\partial t} + \frac{m_0\,|\boldsymbol{u}|^2}{2}\frac{\partial n}{\partial t} + m_0 n \boldsymbol{u} \cdot \frac{\partial \boldsymbol{u}}{\partial t} = \frac{\partial \hat{e}}{\partial t} - \frac{m_0\,|\boldsymbol{u}|^2}{2}\frac{\partial n}{\partial t} + m_0 \boldsymbol{u} \cdot \frac{\partial (n\boldsymbol{u})}{\partial t}. \tag{2.17}$$

Direct calculations lead to

$$\begin{aligned} \nabla \cdot (e_{tot}\boldsymbol{u}) &= \nabla \cdot \left(\left(\hat{e} + \frac{m_0 n}{2}\,|\boldsymbol{u}|^2 \right) \boldsymbol{u} \right) \\ &= \nabla \cdot (\hat{e}\boldsymbol{u}) + \frac{m_0 n\,|\boldsymbol{u}|^2}{2} \nabla \cdot \boldsymbol{u} + \frac{m_0\,|\boldsymbol{u}|^2}{2} \boldsymbol{u} \cdot \nabla n + m_0 n \boldsymbol{u} \cdot \big((\boldsymbol{u} \cdot \nabla)\boldsymbol{u} \big) \\ &= \nabla \cdot (\hat{e}\boldsymbol{u}) - \frac{m_0\,|\boldsymbol{u}|^2}{2} \nabla \cdot (n\boldsymbol{u}) + m_0 \boldsymbol{u} \cdot \big(\nabla \cdot (n\boldsymbol{u}\boldsymbol{u}) \big). \end{aligned} \tag{2.18}$$

Substituting the above two equations into (2.5) yields

$$\begin{aligned} &\frac{\partial \hat{e}}{\partial t} + \nabla \cdot (\hat{e}\boldsymbol{u}) - \frac{m_0\,|\boldsymbol{u}|^2}{2} \left(\frac{\partial n}{\partial t} + \nabla \cdot (n\boldsymbol{u}) \right) + m_0 \boldsymbol{u} \cdot \left(\frac{\partial (n\boldsymbol{u})}{\partial t} + \nabla \cdot (n\boldsymbol{u}\boldsymbol{u}) \right) \\ &\quad = \nabla \cdot (\hat{\boldsymbol{\sigma}}\boldsymbol{u}) - \nabla \cdot \boldsymbol{j}_e. \end{aligned} \tag{2.19}$$

When combined with (2.3) and (2.4), the above equation reduces to

$$\frac{\partial \hat{e}}{\partial t} + \nabla \cdot (\hat{e}\boldsymbol{u}) = \hat{\boldsymbol{\sigma}} : \nabla \boldsymbol{u} - \nabla \cdot \boldsymbol{j}_e, \tag{2.20}$$

where we have used the relation $\nabla \cdot (\hat{\boldsymbol{\sigma}}\boldsymbol{u}) = (\nabla \cdot \hat{\boldsymbol{\sigma}}) \cdot \boldsymbol{u} + \hat{\boldsymbol{\sigma}} : \nabla \boldsymbol{u}$.

By substituting (2.20) into (2.17) and integrating by parts, we have

$$\begin{aligned} \dot{\mathcal{S}} = &\int_\Omega \left(\left(\nabla \cdot \left(\frac{M}{T} \nabla n \right) + \frac{\partial s}{\partial n} \right) \frac{\partial n}{\partial t} + \frac{1}{T} \big(-\nabla \cdot (\hat{e}\boldsymbol{u}) - \nabla \cdot \boldsymbol{j}_e + \hat{\boldsymbol{\sigma}} : \nabla \boldsymbol{u} \big) \right) \mathrm{d}x \\ &+ \int_{\Gamma_S} \left(-\frac{M}{T}\frac{\partial n}{\partial \boldsymbol{v}}\frac{\partial n}{\partial t} + s_b'(n)\,\frac{\partial n}{\partial t} \right) \mathrm{d}A. \end{aligned} \tag{2.21}$$

We introduce a notation on the chemical potential, i.e.

$$\hat{\mu} := -T \left(\frac{\partial s}{\partial n} + \nabla \cdot \left(\frac{M}{T} \nabla n \right) \right). \tag{2.22}$$

https://doi.org/10.1017/jfm.2026.11152 Published online by Cambridge University Press

Then we substitute (2.3) into (2.21) and integrate by parts. This gives

$$\begin{aligned}\dot{\mathcal{S}} &= \int_\Omega \left(\frac{\hat{\mu}}{T}\nabla\cdot(n\boldsymbol{u}) + \frac{1}{T}\big(-\nabla\cdot(\hat{e}\boldsymbol{u}) - \nabla\cdot\boldsymbol{j}_e + \hat{\boldsymbol{\sigma}}:\nabla\boldsymbol{u}\big)\right)\mathrm{d}x \\ &\quad + \int_{\Gamma_S}\left(-\frac{M}{T}\frac{\partial n}{\partial \boldsymbol{v}} + s_b'(n)\right)\frac{\partial n}{\partial t}\,\mathrm{d}A \\ &= \int_\Omega \left(-n\boldsymbol{u}\cdot\nabla\frac{\hat{\mu}}{T} + \hat{e}\boldsymbol{u}\cdot\nabla\frac{1}{T} + \boldsymbol{j}_e\cdot\nabla\frac{1}{T} - \nabla\cdot\left(\frac{\hat{\boldsymbol{\sigma}}}{T}\right)\cdot\boldsymbol{u}\right)\mathrm{d}x \\ &\quad + \int_{\Gamma_S}\left(\frac{1}{T}\boldsymbol{u}_\tau\cdot(\boldsymbol{P}\hat{\boldsymbol{\sigma}}\boldsymbol{v}) - \frac{\boldsymbol{j}_e\cdot\boldsymbol{v}}{T} + \left(-\frac{M}{T}\frac{\partial n}{\partial \boldsymbol{v}} + s_b'(n)\right)\frac{\partial n}{\partial t}\right)\mathrm{d}A. \end{aligned} \tag{2.23}$$

In the derivation, we have used the relation $\boldsymbol{u}\cdot\boldsymbol{v}=0$ and the notation for the tangential projection operator $\boldsymbol{P}=\boldsymbol{I}-\boldsymbol{v}\boldsymbol{v}$.

We then compute the entropy production rate $\dot{\mathcal{S}}_{prod}$ in the whole system:

$$\begin{aligned}\dot{\mathcal{S}}_{prod} &= \dot{\mathcal{S}} + \int_{\Gamma_S}\frac{\boldsymbol{j}_{e,s}\cdot\boldsymbol{v}}{T}\,\mathrm{d}A - \int_{\Gamma_S}\frac{1}{T}\boldsymbol{P}\hat{\boldsymbol{\sigma}}\boldsymbol{v}\cdot\boldsymbol{u}_\tau\,\mathrm{d}A \\ &= \int_\Omega\left(\boldsymbol{u}\cdot\left(-n\,\nabla\frac{\hat{\mu}}{T} + \hat{e}\,\nabla\frac{1}{T} - \nabla\cdot\left(\frac{\hat{\boldsymbol{\sigma}}}{T}\right)\right) + \boldsymbol{j}_e\cdot\nabla\frac{1}{T}\right)\mathrm{d}x \\ &\quad + \int_{\Gamma_S}\left(-\frac{(\boldsymbol{j}_e-\boldsymbol{j}_{e,s})\cdot\boldsymbol{v}}{T} + \left(-\frac{M}{T}\frac{\partial n}{\partial \boldsymbol{v}} + s_b'(n)\right)\frac{\partial n}{\partial t}\right)\mathrm{d}A =: I_1 + I_2. \end{aligned} \tag{2.24}$$

The first term I_1 on the right-hand side of the equation is already a linear functional with respect to $\boldsymbol{u}$ and $\boldsymbol{j}_e$. We further compute the second term I_2. By substituting (2.7) into I_2 and integrating by parts, we obtain

$$\begin{aligned} I_2 &= \int_{\Gamma_S}\left(-\frac{1}{T}\left(e_b'(n)\,\frac{\partial n}{\partial t} + \nabla_\Gamma\cdot(e_b\boldsymbol{u}_\tau)\right) + \left(-\frac{M}{T}\frac{\partial n}{\partial \boldsymbol{v}} + s_b'(n)\right)\frac{\partial n}{\partial t}\right)\mathrm{d}A \\ &= \int_{\Gamma_S}\left(-\frac{1}{T}\,\nabla_\Gamma\cdot(e_b\boldsymbol{u}_\tau) - \frac{1}{T}\left(M\frac{\partial n}{\partial \boldsymbol{v}} + e_b'(n) - T\,s_b'(n)\right)\frac{\partial n}{\partial t}\right)\mathrm{d}A \\ &= \int_{\Gamma_S}\left(-\frac{1}{T^2}\,\nabla_\Gamma T\cdot(e_b\boldsymbol{u}_\tau) - \frac{L(n)}{T}\dot{n} + \frac{L(n)}{T}\boldsymbol{u}_\tau\cdot\nabla_\Gamma n\right)\mathrm{d}A. \end{aligned} \tag{2.25}$$

Here, in the last equation, we have used $\dot{n}=\partial n/\partial t + \boldsymbol{u}_\tau\cdot\nabla_\Gamma n$ on Γ_S, and $L(n):=M(\partial n/\partial\boldsymbol{v}) + e_b'(n) - T\,s_b'(n)$. Notice that the Helmholtz free energy on the surface can be defined as $f_b=e_b-Ts_b$. Then we have $L(n)=M(\partial n/\partial\boldsymbol{v}) + \partial f_b(n,T)/\partial n|_T$. Substituting the expression for I_2 in (2.24) gives

$$\begin{aligned}\dot{\mathcal{S}}_{prod} &= \int_\Omega\left(\boldsymbol{u}\cdot\left(-n\,\nabla\frac{\hat{\mu}}{T} + \hat{e}\,\nabla\frac{1}{T} - \nabla\cdot\left(\frac{\hat{\boldsymbol{\sigma}}}{T}\right)\right) + \boldsymbol{j}_e\cdot\nabla\frac{1}{T}\right)\mathrm{d}x \\ &\quad + \int_{\Gamma_S}\left(-\frac{e_b}{T^2}\,\nabla_\Gamma T + \frac{L(n)}{T}\,\nabla_\Gamma n\right) - \frac{L(n)}{T}\dot{n}\right)\mathrm{d}A. \end{aligned} \tag{2.26}$$

Now we see that $\dot{\mathcal{S}}_{prod}$ is reduced to a linear functional with respect to $\boldsymbol{u}$, $\boldsymbol{j}_e$, $\boldsymbol{u}_\tau|_{\Gamma_S}$ and $\dot{n}|_{\Gamma_S}$.

Based on the above results, the constraint optimisation problem (2.16) is reduced to an unconstrained one, i.e.

$$\min_{\boldsymbol{u},\boldsymbol{j}_e,\boldsymbol{u}_\tau|_{\Gamma_S},\dot{n}|_{\Gamma_S}} \mathcal{R} = \Phi - \dot{\mathcal{S}}_{prod}. \tag{2.27}$$

https://doi.org/10.1017/jfm.2026.11152 Published online by Cambridge University Press

From (2.14), we see that Φ is a quadratic functional with respect to $\boldsymbol{u}$, $\boldsymbol{j}_e$, $\boldsymbol{u}_\tau|_{\Gamma_S}$ and $\dot{n}|_{\Gamma_S}$. It is easy to know that the Rayleigh functional $\mathcal{R}(\boldsymbol{u}, \boldsymbol{j}_e, \dot{n}|_{\Gamma_S}, \boldsymbol{u}_\tau|_{\Gamma_S})$ has a unique minimiser, which is derived by setting the first derivatives of $\mathcal{R}$ to be zero. Direct calculations give

$$\delta\Phi = \int_\Omega -\nabla\cdot\frac{\boldsymbol{\sigma}}{T}\cdot\delta\boldsymbol{u} + \frac{\boldsymbol{j}_e\cdot\delta\boldsymbol{j}_e}{\lambda T^2}\,\mathrm{d}x + \int_{\Gamma_S}\frac{1}{T}(\alpha\boldsymbol{u}_\tau + \boldsymbol{P}\boldsymbol{\sigma}\boldsymbol{v})\cdot\delta\boldsymbol{u}_\tau + \frac{\beta}{T}\dot{n}\cdot\delta\dot{n}\,\mathrm{d}A, \tag{2.28}$$

where $\boldsymbol{\sigma}$ is the dissipative stress tensor defined as

$$\boldsymbol{\sigma} := \left(\eta\left(\nabla\boldsymbol{u} + \nabla\boldsymbol{u}^{\mathrm{T}}\right) + \left(\xi - \frac{2\eta}{d}\right)\nabla\cdot\boldsymbol{u}\boldsymbol{I}\right). \tag{2.29}$$

In the end, we derive the following constitutive equations and boundary conditions:

$$\frac{\delta\mathcal{R}}{\delta\boldsymbol{j}_e} = 0 \quad\Rightarrow\quad \boldsymbol{j}_e = -\lambda\nabla T \quad \text{in } \Omega, \tag{2.30}$$

$$\frac{\delta\mathcal{R}}{\delta\boldsymbol{u}} = 0 \quad\Rightarrow\quad \nabla\cdot\left(\frac{1}{T}\hat{\boldsymbol{\sigma}}\right) = \nabla\cdot\left(\frac{1}{T}\boldsymbol{\sigma}\right) - \left(n\,\nabla\frac{\hat{\mu}}{T} - \hat{e}\,\nabla\frac{1}{T}\right) \quad \text{in } \Omega, \tag{2.31}$$

$$\frac{\delta\mathcal{R}}{\delta\boldsymbol{u}_\tau|_{\Gamma_S}} = 0 \quad\Rightarrow\quad \beta\dot{n} + L(n) = 0 \quad \text{on } \Gamma_S, \tag{2.32}$$

$$\frac{\delta\mathcal{R}}{\delta\dot{n}|_{\Gamma_S}} = 0 \quad\Rightarrow\quad \alpha\boldsymbol{u}_\tau + \boldsymbol{P}\boldsymbol{\sigma}\boldsymbol{v} - \frac{e_b}{T}\nabla_\Gamma T - L(n)\nabla_\Gamma n = 0 \quad \text{on } \Gamma_S. \tag{2.33}$$

To further simplify (2.31), we use the expression for pressure $\hat{p} := n\hat{\mu} - \hat{e} + T\hat{s}$ (Onuki 2007). In the following, we will show that $n\,\nabla(\hat{\mu}/T) - \hat{e}\,\nabla(1/T)$ can be rewritten as a divergence form. Notice that $\hat{\mu} = -T((\partial s/\partial n) + \nabla\cdot((M/T)\,\nabla n)) = \mu - T\,\nabla\cdot((M/T)\,\nabla n)$, where we denote $\mu = -T(\partial s/\partial n)$ for simplicity in expressions. Direct calculations give

$$\begin{aligned}\hat{p} &= n(\mu - T\nabla\cdot\left(\frac{M}{T}\nabla n\right)) - e - \frac{K}{2}|\nabla n|^2 + T\left(s - \frac{C}{2}|\nabla n|^2\right)\\ &= n\mu - e + Ts - nT\,\nabla\cdot\left(\frac{M}{T}\nabla n\right) - \frac{M}{2}|\nabla n|^2\\ &= p - nT\,\nabla\cdot\left(\frac{M}{T}\nabla n\right) - \frac{M}{2}|\nabla n|^2.\end{aligned} \tag{2.34}$$

Here, we set $p = n\mu - e + Ts$. By the definition of T and μ, we easily have $\nabla s = -(\mu/T)\,\nabla n + (1/T)\,\nabla e$. This further leads to

$$\nabla\cdot\left(\frac{p}{T}\boldsymbol{I}\right) = \nabla\frac{p}{T} = -e\,\nabla\frac{1}{T} + n\,\nabla\frac{\mu}{T}. \tag{2.35}$$

Direct calculations yield

$$\begin{aligned}\nabla\cdot\left(\frac{1}{T}\hat{p}\boldsymbol{I}\right) &= \nabla\frac{\hat{p}}{T} = \nabla\left(\frac{p}{T} - n\,\nabla\cdot\left(\frac{M}{T}\nabla n\right) - \frac{M}{2T}|\nabla n|^2\right)\\ &= \nabla\frac{p}{T} - n\,\nabla\left(\nabla\cdot\left(\frac{M}{T}\nabla n\right)\right) - \left(\nabla\cdot\left(\frac{M}{T}\nabla n\right)\right)\nabla n\\ &\quad - \frac{M}{2T}\nabla|\nabla n|^2 - |\nabla n|^2\,\nabla\frac{M}{2T}\end{aligned}$$

https://doi.org/10.1017/jfm.2026.11152 Published online by Cambridge University Press

$$= \nabla \frac{p}{T} - n \nabla \left(\nabla \cdot \left(\frac{M}{T} \nabla n \right) \right) - \nabla \cdot \left(\frac{M}{T} \nabla n \nabla n \right) - \frac{|\nabla n|^2}{2} \nabla \left(\frac{K}{T} + C \right)$$
$$= n \nabla \frac{\mu}{T} - e \nabla \frac{1}{T} - n \nabla \nabla \cdot \left(\frac{M}{T} \nabla n \right) - \frac{K}{2} |\nabla n|^2 \nabla \frac{1}{T} - \nabla \cdot \left(\frac{M}{T} \nabla n \nabla n \right)$$
$$= n \nabla \frac{\hat{\mu}}{T} - \hat{e} \nabla \frac{1}{T} - \nabla \cdot \left(\frac{M}{T} \nabla n \nabla n \right). \tag{2.36}$$

Thus we have

$$n \nabla \frac{\hat{\mu}}{T} - \hat{e} \nabla \frac{1}{T} = \nabla \cdot \left(\frac{1}{T} \boldsymbol{\Pi} \right), \tag{2.37}$$

where

$$\boldsymbol{\Pi} := \hat{p} \boldsymbol{I} + M \nabla n \nabla n. \tag{2.38}$$

The tensor $\boldsymbol{\Pi}$ is the reversible stress tensor containing the gradient contributions (Onuki 2007). By substituting (2.37) into (2.31), we have

$$\hat{\boldsymbol{\sigma}} = \boldsymbol{\sigma} - \boldsymbol{\Pi}, \tag{2.39}$$

where $\boldsymbol{\sigma}$ is the standard viscous stress defined in (2.29), and $\boldsymbol{\Pi}$ is given in (2.38).

2.5. *The two-phase flow equations*

Previously, we have derived the constitutive equations (2.30) and (2.39) together with the boundary conditions (2.32) and (2.33) by using the extended Onsager principle. We substitute them into the momentum conservation equation (2.4) and the energy conservation equation (2.5). By combining all the conservation equations and the boundary conditions, we derive a complete system for the one-component two-phase flows:

$$\begin{cases} \dfrac{\partial n}{\partial t} + \nabla \cdot (n \boldsymbol{u}) = 0 & \text{in } \Omega, \quad (2.40) \\ m_0 \left(\dfrac{\partial n \boldsymbol{u}}{\partial t} + \nabla \cdot (n \boldsymbol{u} \boldsymbol{u}) \right) = \nabla \cdot (\boldsymbol{\sigma} - \boldsymbol{\Pi}) & \text{in } \Omega, \quad (2.41) \\ \dfrac{\partial e_{tot}}{\partial t} + \nabla \cdot (e_{tot} \boldsymbol{u}) = \nabla \cdot ((\boldsymbol{\sigma} - \boldsymbol{\Pi}) \boldsymbol{u}) + \nabla \cdot (\lambda \nabla T) & \text{in } \Omega, \quad (2.42) \\ \boldsymbol{u} \cdot \boldsymbol{\nu} = 0, \quad \alpha \boldsymbol{u}_\tau + \boldsymbol{P} \boldsymbol{\sigma} \boldsymbol{\nu} + \dfrac{e_b}{T} \nabla_\Gamma T - L(n) \nabla_\Gamma n = 0 & \text{on } \Gamma_S, \quad (2.43) \\ \beta \left(\dfrac{\partial n}{\partial t} + \boldsymbol{u}_\tau \cdot \nabla_\Gamma n \right) + L(n) = 0 & \text{on } \Gamma_S, \quad (2.44) \\ e_b'(n) \dfrac{\partial n}{\partial t} + \nabla_\Gamma \cdot (e_b \boldsymbol{u}_\tau) = -\lambda \nabla T \cdot \boldsymbol{\nu} - \boldsymbol{j}_{e,s} \cdot \boldsymbol{\nu} & \text{on } \Gamma_S, \quad (2.45) \end{cases}$$

where

$$e_{tot} = e + \frac{K}{2} |\nabla n|^2 + \frac{m_0 n}{2} |\boldsymbol{u}|^2, \quad \boldsymbol{\sigma} = \left(\eta \left(\nabla \boldsymbol{u} + \nabla \boldsymbol{u}^{\mathrm{T}} \right) + \left(\xi - \frac{2\eta}{d} \right) \nabla \cdot \boldsymbol{u} \boldsymbol{I} \right),$$
$$\boldsymbol{\Pi} = \hat{p} \boldsymbol{I} + M \nabla n \nabla n, \quad \frac{1}{T} = \frac{\partial s(n, e)}{\partial e}, \quad \hat{p} = n \hat{\mu} - \hat{e} + T \hat{s},$$
$$\hat{\mu} = -T \left(\frac{\partial s}{\partial n} + \nabla \cdot \left(\frac{M}{T} \nabla n \right) \right), \quad L(n) = M \frac{\partial n}{\partial \boldsymbol{\nu}} + \frac{\partial f_s(n, T)}{\partial n}. \tag{2.46}$$

https://doi.org/10.1017/jfm.2026.11152 Published online by Cambridge University Press

Let $n(x,t)$, $\boldsymbol{u}$ and $e(x,t)$ be the solutions of the system (2.40)–(2.45) for given initial values. If we substitute (2.30)–(2.33) into (2.26), integration by parts leads to

$$\frac{\mathrm{d}\mathcal{S}_{prod}}{\mathrm{d}t} = 2\Phi(\boldsymbol{u},\, \boldsymbol{j}_e,\, \boldsymbol{u}_\tau|_{\Gamma_S},\, \dot{n}|_{\Gamma_S}) \geqslant 0. \tag{2.47}$$

The term Φ is non-negative by definition.

Instead of (2.42), we can also derive the equation for $\hat{e} = e + (K/2)\,|\nabla n|^2$, i.e.

$$\frac{\partial \hat{e}}{\partial t} + \nabla\cdot(\hat{e}\boldsymbol{u}) = (\boldsymbol{\sigma} - \boldsymbol{\Pi}) : \nabla\boldsymbol{u} + \nabla\cdot(\lambda\,\nabla T). \tag{2.48}$$

Equation (2.42) can also be replaced by an equation for entropy,

$$\frac{\partial \hat{s}}{\partial t} + \nabla\cdot(\hat{s}\boldsymbol{u}) = -\nabla\cdot\widehat{\boldsymbol{J}} + \frac{1}{T}\boldsymbol{\sigma} : \nabla\boldsymbol{u} + \frac{\boldsymbol{j}_e}{T^2}\cdot\nabla T, \tag{2.49}$$

where $\widehat{\boldsymbol{J}} = [M\,\nabla n(\partial n/\partial t + \boldsymbol{u}\cdot\nabla n) - \boldsymbol{j}_e]/T$.

When the solid boundary is adiabatic, i.e. $\boldsymbol{j}_{e,s} = 0$, (2.45) actually gives a Neumann-type boundary condition for the temperature T. In many situations, we fix the temperature of the boundary, then (2.45) will be replaced by a Dirichlet boundary condition $T(x,t)|_{\Gamma_S} = T_s(x,t)$. When α goes to infinity, the boundary condition (2.43) will reduce to the standard no-slip boundary condition $\boldsymbol{u} = 0$ on Γ_S. When β goes to zero, condition (2.44) will reduce to $L(n) = 0$, i.e. $M(\partial n/\partial \boldsymbol{\nu}) = -\partial f_s/\partial n$. This corresponds to the Young's equation for the equilibrium contact angle. In applications, the slip coefficient α can be directly obtained from molecular dynamics simulations (Qian *et al.* 2003; Lācis *et al.* 2020, 2022). The phenomenological relaxation parameter β can be chosen by optimally matching the flow field with that in molecular dynamics simulations (see more details in Qian *et al.* 2003).

2.6. *Reformulation for the system*

To facilitate the derivation of the lattice Boltzmann scheme, we reformulate the system (2.40)–(2.45) as follows. First, we will use $\rho = m_0 n$ as the fundamental unknown instead of n. Consequently, the mass equation (2.40) is reformulated to

$$\frac{\partial \rho}{\partial t} + \nabla\cdot(\rho\boldsymbol{u}) = 0. \tag{2.50}$$

Notice the relation $\nabla\cdot((1/T)(\hat{p}\boldsymbol{I} + M\,\nabla n\,\nabla n)) = n\,\nabla(\hat{\mu}/T) - \hat{e}\,\nabla(1/T)$. By the definition $\hat{p} = n\hat{\mu} - \hat{e} + T\hat{s}$, direct calculations lead to the relation

$$\nabla\hat{p} + \nabla\cdot M(\nabla n\,\nabla n) = n\,\nabla\hat{\mu} + \hat{s}\,\nabla T + \frac{1}{T}M(\nabla n\cdot\nabla T)\,\nabla T. \tag{2.51}$$

Using this equation, the momentum (2.4) can be regrouped as

$$\frac{\partial \rho\boldsymbol{u}}{\partial t} + \nabla\cdot(\rho\boldsymbol{u}\boldsymbol{u}) = -n\,\nabla\hat{\mu} - \hat{s}\,\nabla T - \frac{1}{T}M(\nabla n\cdot\nabla T)\,\nabla T + \nabla\cdot\boldsymbol{\sigma}. \tag{2.52}$$

In addition, the total energy transport (2.42) can be rewritten as

$$\begin{aligned}
\frac{\partial e_{tot}}{\partial t} + \nabla\cdot(e_{tot}\boldsymbol{u}) &= -\nabla\cdot((\hat{p}\boldsymbol{I} + M\,\nabla n\,\nabla n)\cdot\boldsymbol{u}) + \nabla\cdot(\boldsymbol{\sigma}\cdot\boldsymbol{u}) + \nabla\cdot(\lambda\,\nabla T)\\
&= -(\hat{p}\boldsymbol{I} + M\,\nabla n\,\nabla n) : \nabla\boldsymbol{u} - \boldsymbol{u}\cdot\nabla\cdot(\hat{p}\boldsymbol{I} + M\,\nabla n\,\nabla n) + \nabla\cdot(\boldsymbol{\sigma}\cdot\boldsymbol{u}) + \nabla\cdot(\lambda\,\nabla T)\\
&= -(\hat{p}\boldsymbol{I} + M\,\nabla n\,\nabla n) : \nabla\boldsymbol{u} + \nabla\cdot(\boldsymbol{\sigma}\cdot\boldsymbol{u}) + \nabla\cdot(\lambda\,\nabla T)\\
&\quad - \boldsymbol{u}\cdot(n\,\nabla\hat{\mu} + \hat{s}\,\nabla T + \frac{1}{T}M(\nabla n\cdot\nabla T)\,\nabla T).
\end{aligned} \tag{2.53}$$

The boundary conditions can also be updated accordingly.

https://doi.org/10.1017/jfm.2026.11152 Published online by Cambridge University Press

2.7. *Discussions*

To conclude this section, we remark on the connections between the variational approach and classical methods in the literature – e.g. Guo & Lin (2015), Magaletti *et al.* (2016), Kou & Sun (2018*a*) and Gallo *et al.* (2020) for non-isothermal systems, and Ren & E (2011) and Magaletti *et al.* (2022) for isothermal cases. The classical approach begins with the conservation equations and assumes that the system is in a linear response regime. Constitutive relations are then derived by analysing the entropy production rate and invoking the Clausius–Duhem inequality. In principle, these approaches can yield identical systems of equations, provided that all reversible and irreversible terms are properly specified. While the classical approach is well suited for isothermal systems or those with simple thermomechanical coupling, it requires the careful application of various thermodynamic relations for more complex scenarios (Onuki 2007). In contrast, the extended Onsager principle provides a unified framework for handling systems with diverse effects – such as wetting, phase transition and cross-diffusion in multi-component fluids. This approach starts from the definition of the Rayleigh functional, from which the constitutive and thermodynamic relations are derived directly through variational calculus. The resulting system automatically satisfies the Onsager reciprocal relations and the second law of thermodynamics.

We now distinguish the present model in (2.40)–(2.45) from other models in the literature. A key difference lies in the formulation of the heat flux. In our model, the heat flux is proportional to the temperature gradient, with the effect of the density gradient implicitly handled by the coupled system. In contrast, the models proposed by Magaletti *et al.* (2016) and Gallo *et al.* (2020) explicitly incorporate a mass gradient term in the heat flux. Furthermore, our model differs from the quasi-incompressible models in Guo & Lin (2015) and Sun *et al.* (2024). Those works employ a phase-field function within a Cahn–Hilliard framework to describe phase separation. Our model, however, is developed within a fully compressible framework and is capable of describing both phase separation and phase transitions in a single-component, two-phase flow system.

3. The lattice Boltzmann model

This section develops an LBM for the aforementioned non-isothermal two-phase fluid system described by (2.50)–(2.53). We first introduce a discrete velocity model (DVM) by discretising the velocity space of the underlying continuous kinetic equations into a finite set of discrete velocities. Chapman–Enskog analysis confirms that this DVM accurately approximates the two-phase fluid system. The lattice Boltzmann model is subsequently derived by applying standard numerical schemes to discretise the temporal and spatial derivatives of the DVM.

3.1. *The well-balanced discrete velocity kinetic model for velocity distribution function*

Building upon the established kinetic model for decoupled hydrodynamic and energy equations in Guo *et al.* (2007), and inspired by the well-balanced LBM for two-phase flow (Guo 2021), we develop a discrete velocity kinetic model for non-isothermal two-phase flow through appropriate modifications to the source distribution functions, as detailed below.

The evolution equations of the DVM for velocity distribution function read

$$\partial_t f_i + \boldsymbol{c}_i \cdot \nabla f_i = -\frac{1}{\tau_f}\left(f_i - f_i^{eq}\right) + F_i, \tag{3.1}$$

https://doi.org/10.1017/jfm.2026.11152 Published online by Cambridge University Press

where f_i is the velocity distribution function after the discretisation of the molecule velocity space, and f_i^{eq} is the modified local equilibrium distribution function, defined as

$$f_i^{eq} = \begin{cases} \rho - (1-\omega_0)\rho_0/(RT_0) + \omega_0 s_0(\boldsymbol{u}), & i = 0, \\ \omega_i \rho_0/(RT_0) + s_i(\boldsymbol{u}), & i \neq 0. \end{cases} \tag{3.2}$$

Here, $s_i(\boldsymbol{u}) = \omega_i((\boldsymbol{c}_i \cdot (\rho \boldsymbol{u})/RT_0) + ((\rho \boldsymbol{u}\boldsymbol{u}) : (\boldsymbol{c}_i\boldsymbol{c}_i - c_s^2 \boldsymbol{I})/2(RT_0)^2))$, R is the gas constant, T_0 is the reference temperature, ρ_0 is a numerical constant, and the weights ω_i can be found in the Appendix of Guo (2021). In our simulation, the value of ρ_0 is set to 0 for simplicity. Also, F_i is the force term defined as

$$F_i = \omega_i \left(\frac{\boldsymbol{c}_i \cdot \boldsymbol{F}_{non}}{RT_0} + \frac{\boldsymbol{u}(\boldsymbol{F}_{non} + c_s^2 \nabla \rho) : (\boldsymbol{c}_i\boldsymbol{c}_i - RT_0 \boldsymbol{I})}{(RT_0)^2} + \frac{1}{2}\left(\frac{|\boldsymbol{c}_i|^2}{RT_0} - d \right)(\boldsymbol{u} \cdot \nabla \rho) \right), \tag{3.3}$$

where $\boldsymbol{F}_{non} = -n \nabla \hat{\mu} - \hat{s} \nabla T - (1/T) M (\nabla n \cdot \nabla T) \nabla T$.

By using the isotropic constraints, the following moments can be obtained:

$$\begin{cases} \sum_i f_i^{eq} = \sum_i f_i = \rho, \\ \sum_i \boldsymbol{c}_i f_i^{eq} = \sum_i \boldsymbol{c}_i f_i = \rho \boldsymbol{u}, \\ \sum_i \boldsymbol{c}_i \boldsymbol{c}_i f_i^{eq} = \rho_0 \boldsymbol{I} + \rho \boldsymbol{u}\boldsymbol{u}, \\ \sum_i \boldsymbol{c}_i \boldsymbol{c}_i \boldsymbol{c}_i f_i^{eq} = RT_0 \rho [\boldsymbol{u}\boldsymbol{I}], \\ \sum_i F_i(\boldsymbol{x}, t) = 0, \\ \sum_i \boldsymbol{c}_i F_i(\boldsymbol{x}, t) = \boldsymbol{F}_{non}, \\ \sum_i \boldsymbol{c}_i \boldsymbol{c}_i F_i = [\boldsymbol{u}\boldsymbol{F}_{non}] + RT_0 [\boldsymbol{u} \nabla \rho] + RT_0 \boldsymbol{u} \cdot \nabla \rho \boldsymbol{I}, \end{cases} \tag{3.4}$$

where $[\boldsymbol{u}\boldsymbol{I}]_{\alpha\beta\gamma} = u_\alpha \delta_{\beta\gamma} + u_\beta \delta_{\alpha\gamma} + u_\gamma \delta_{\alpha\beta}$, $[\boldsymbol{u}\boldsymbol{F}]_{\alpha\beta} = u_\alpha F_\beta + u_\beta F_\alpha$ and $[\boldsymbol{u} \nabla \rho]_{\alpha\beta} = u_\alpha \partial_\beta \rho + u_\beta \partial_\alpha \rho$.

3.2. *Chapman–Enskog analysis of the well-balanced discrete velocity kinetic model*

We will derive the equations satisfied by the moments (3.4) by Chapman–Enskog analysis. We introduce the following Chapman–Enskog expansions for the evolution (3.1):

$$\partial_t = \varepsilon \partial_{t_1} + \varepsilon^2 \partial_{t_2} + \cdots, \quad \nabla = \varepsilon \nabla_1, \quad F_i = \varepsilon F_i^{(1)}, \tag{3.5}$$

$$f_i = f_i^0 + \varepsilon f_i^{(1)} + \varepsilon^2 f_i^{(2)} + \cdots. \tag{3.6}$$

Here, ε is a small parameter proportional to the Knudsen number, $t_1 = \varepsilon t$, $t_2 = \varepsilon^2 t$ and $x_1 = \varepsilon x$ are corresponding macroscopic scales, and $\nabla_1 = (\partial_{x_1}, \partial_{y_1}, \partial_{z_1})$.

Substituting the expansions into (3.1) yields the following equations at different scales:

$$\text{for } O(\varepsilon), \quad \partial_{t_1} f_i^{(0)} + \boldsymbol{c}_i \cdot \nabla_1 f_i^{(0)} = -\frac{1}{\tau_f} f_i^{(1)} + F_i^{(1)}, \tag{3.7}$$

$$\text{for } O(\varepsilon^2), \quad \partial_{t_2} f_i^{(0)} + \partial_{t_1} f_i^{(1)} + \boldsymbol{c}_i \cdot \nabla_1 f_i^{(1)} = -\frac{1}{\tau_f} f_i^{(2)}. \tag{3.8}$$

Before recovering the macroscopic equation, the following equations are derived from the first two equations of the moment system (3.4):

$$\sum_i f_i^{(0)} = \rho, \quad \sum_i c_i f_i^{(0)} = \rho \boldsymbol{u}. \tag{3.9}$$

https://doi.org/10.1017/jfm.2026.11152 Published online by Cambridge University Press

By taking the zeroth- and first-order velocity moments of (3.7), we obtain the following hydrodynamic equations at $O(\varepsilon)$:

$$\frac{\partial \rho}{\partial t_1} + \nabla_1 \cdot (\rho \boldsymbol{u}) = 0, \tag{3.10}$$

$$\frac{\partial (\rho \boldsymbol{u})}{\partial t_1} + \nabla_1 \cdot (\rho_0 \boldsymbol{I} + \rho \boldsymbol{u}\boldsymbol{u}) = \boldsymbol{F}_{non}^{(1)}. \tag{3.11}$$

Similarly, by taking the zeroth- and first-order velocity moments of (3.8), we get the hydrodynamic equations at $O(\varepsilon^2)$:

$$\frac{\partial \rho}{\partial t_2} = 0, \tag{3.12}$$

$$\frac{\partial (\rho \boldsymbol{u})}{\partial t_2} + \nabla_1 \cdot \sum_i \boldsymbol{c}_i \boldsymbol{c}_i f_i^{(1)} = 0. \tag{3.13}$$

From (3.7), we have

$$\begin{aligned} -\frac{1}{\tau_f} \sum_i \boldsymbol{c}_i \boldsymbol{c}_i f_i^{(1)} &= \partial_{t_1} (\rho_0 \boldsymbol{I} + \rho \boldsymbol{u}\boldsymbol{u}) + \nabla_1 \cdot (RT_0 \rho [\boldsymbol{u}\boldsymbol{I}]) - \left[\boldsymbol{u}\boldsymbol{F}_{non}^{(1)}\right] \\ &\quad - RT_0 [\boldsymbol{u}\, \nabla_1 \rho] - RT_0 \boldsymbol{u} \cdot \nabla_1 \rho \boldsymbol{I} \\ &= RT_0 \rho (\nabla_1 \boldsymbol{u} + \nabla_1 \boldsymbol{u}^{\mathrm{T}} + \nabla_1 \cdot (\boldsymbol{u}\boldsymbol{I})) + O\left(\boldsymbol{u}^3\right), \end{aligned} \tag{3.14}$$

where we have used the expressions

$$\begin{aligned} \partial_{t_1} (\rho u_\alpha u_\beta) &= \rho u_\alpha\, \partial_{t_1} u_\beta + u_\beta\, \partial_{t_1} (\rho u_\alpha) \\ &= u_\alpha F_{non\beta}^{(1)} - u_\alpha u_\beta\, \partial_{t_1} \rho - u_\alpha\, \nabla_{1\beta} (\rho u_\beta u_\gamma) + u_\beta F_{non\alpha}^{(1)} - u_\beta \nabla_{1\alpha} (\rho u_\alpha u_\gamma) \\ &= \left[\boldsymbol{u}\boldsymbol{F}_{non}^{(1)}\right] + u_\alpha u_\beta \nabla_{1\gamma} \rho u_\gamma - u_\alpha \nabla_{1\beta} (\rho u_\beta u_\gamma) - u_\beta\, \nabla_{1\alpha} (\rho u_\alpha u_\gamma) \\ &= \left[\boldsymbol{u}\boldsymbol{F}_{non}^{(1)}\right] - \nabla_1 \cdot (\rho \boldsymbol{u}\boldsymbol{u}\boldsymbol{u}) \end{aligned} \tag{3.15}$$

and

$$\begin{aligned} \nabla_1 \cdot (RT_0 \rho [\boldsymbol{u}\boldsymbol{I}]) &= \nabla_{1\alpha} (RT_0 \rho (u_\alpha \delta_{\beta\gamma} + u_\beta \delta_{\alpha\gamma} + u_\gamma \delta_{\alpha\beta})) \\ &= \nabla_{1\alpha} (RT_0 \rho u_\alpha \delta_{\beta\gamma}) + \nabla_{1\gamma} (RT_0 \rho u_\beta) + \nabla_{1\beta} (RT_0 \rho u_\gamma). \end{aligned} \tag{3.16}$$

Substituting (3.14) into (3.13) and enforcing $\eta = RT_0 \tau_f \rho$, we obtain

$$\text{for } O(\varepsilon^2), \quad \frac{\partial (\rho \boldsymbol{u})}{\partial t_2} = \nabla_1 \cdot \eta (\nabla_1 \boldsymbol{u} + \nabla_1 \boldsymbol{u}^{\mathrm{T}} + \nabla_1 \cdot (\boldsymbol{u}\boldsymbol{I})) + O(\boldsymbol{u}^3). \tag{3.17}$$

Combining the equations at both orders $O(\varepsilon)$ and $O(\varepsilon^2)$, the following hydrodynamic equations are recovered:

$$\frac{\partial \rho}{\partial t} + \nabla \cdot (\rho \boldsymbol{u}) = 0, \tag{3.18}$$

$$\frac{\partial \rho \boldsymbol{u}}{\partial t} + \nabla \cdot (\rho \boldsymbol{u}\boldsymbol{u}) = \nabla \cdot \eta (\nabla \boldsymbol{u} + \nabla \boldsymbol{u}^{\mathrm{T}} + \nabla \cdot (\boldsymbol{u}\boldsymbol{I})) + \boldsymbol{F}_{non}. \tag{3.19}$$

Here, the term $O(\boldsymbol{u}^3)$ is not Galilean invariant and is therefore omitted for flows with small Mach numbers.

https://doi.org/10.1017/jfm.2026.11152 Published online by Cambridge University Press

3.3. *The discrete velocity kinetic model for the total energy distribution function*

The evolution equations of the DVM for total energy distribution function h_i read

$$\partial_t h_i + \boldsymbol{c}_i \cdot \nabla h_i = -\frac{1}{\tau_h}(h_i - h_i^{eq}) + \frac{Z_i}{\tau_h}(f_i - f_i^{eq}) + q_i. \tag{3.20}$$

Here, $Z_i = \boldsymbol{c}_i \cdot \boldsymbol{u} - |\boldsymbol{u}|^2/2$, the equilibrium distribution function h_i^{eq} is defined as

$$h_i^{eq} = e_{tot} f_i^{eq} + \omega_i \frac{T}{2}\left(\frac{c_i^2}{(RT_0)^2} - D\right), \tag{3.21}$$

and q_i is the source term distribution function defined as

$$q_i = \omega_i e_{tot} \frac{\boldsymbol{c}_i \cdot \boldsymbol{F}_{non}}{(RT_0)^2} + f_i \boldsymbol{c}_i \cdot \hat{\boldsymbol{F}}, \tag{3.22}$$

where $\hat{\boldsymbol{F}} = \tilde{\boldsymbol{F}} + \boldsymbol{F}_{non}/\rho$, with $\tilde{\boldsymbol{F}} = (((-\hat{p} - Mn_x^2)u_x - Mn_x n_y v_x)/\rho u, (-Mn_x n_y u_y + v_y(-\hat{p} - Mn_y^2))/\rho v)^{\mathrm{T}}$.

Similarly, h_i and q_i satisfy the following moments conditions:

$$\begin{cases} \sum_i h_i^{eq} = \sum_i h_i = e_{tot}, \\ \sum_i \boldsymbol{c}_i h_i^{eq} = e_{tot}\boldsymbol{u}, \\ \sum_i \boldsymbol{c}_i \boldsymbol{c}_i h_i^{eq} = (RT_0)^2 T \boldsymbol{I} + e_{tot}\boldsymbol{u}\boldsymbol{u}, \\ \sum_i q_i = \rho \boldsymbol{u} \cdot \hat{\boldsymbol{F}}, \\ \sum_i \boldsymbol{c}_i q_i = e_{tot}\boldsymbol{F}_{non} + \sum_i \boldsymbol{c}_i \boldsymbol{c}_i f_i \cdot \hat{\boldsymbol{F}}, \\ \sum_i \boldsymbol{c}_i \boldsymbol{c}_i q_i = 0. \end{cases} \tag{3.23}$$

3.4. *Chapman–Enskog analysis of the discrete velocity kinetic model for the total energy distribution function*

As in § 3.2, applying the Chapman–Enskog expansion to the evolution (3.20) yields the following equations at different scales:

$$\text{for } O(\varepsilon), \quad \partial_{t_1} h_i^{(0)} + \boldsymbol{c}_i \cdot \nabla_1 h_i^{(0)} = -\frac{1}{\tau_h} h_i^{(1)} + \frac{Z_k}{\tau_h} f_i^{(1)} + q_i^{(1)}, \tag{3.24}$$

$$\text{for } O(\varepsilon^2), \quad \partial_{t_2} h_i^{(0)} + \partial_{t_1} h_i^{(1)} + \boldsymbol{c}_i \cdot \nabla_1 h_i^{(1)} = -\frac{1}{\tau_h} h_i^{(2)} + \frac{Z_k}{\tau_h} f_i^{(2)} + q_i^{(2)}. \tag{3.25}$$

Similarly, the following equations can be derived from (3.23):

$$\sum_i h_i^{(m)} = 0, \quad m \geqslant 1. \tag{3.26}$$

By taking the zeroth-order moments of (3.24) and (3.25), we obtain the following macroscopic equations at orders $O(\varepsilon)$ and $O(\varepsilon^2)$:

$$\text{for } O(\varepsilon), \quad \frac{\partial e_{tot}}{\partial t_1} + \nabla_1 \cdot (e_{tot}\boldsymbol{u}) = \rho \boldsymbol{u} \cdot \hat{\boldsymbol{F}}^{(1)}, \tag{3.27}$$

$$\text{for } O(\varepsilon^2), \quad \frac{\partial e_{tot}}{\partial t_2} + \nabla_1 \cdot \sum_i \boldsymbol{c}_i h_i^{(1)} = 0. \tag{3.28}$$

https://doi.org/10.1017/jfm.2026.11152 Published online by Cambridge University Press

From (3.24), we obtain

$$-\frac{1}{\tau_h}\sum_i \boldsymbol{c}_i h_i^{(1)} = \partial_{t_1}\sum_i \boldsymbol{c}_i h_i^{eq} + \nabla_1 \cdot \sum_i \boldsymbol{c}_i \boldsymbol{c}_i h_i^{eq} - \frac{1}{\tau_h}\sum_i \boldsymbol{c}_i \boldsymbol{c}_i f_i^{(1)} \cdot \boldsymbol{u} - \sum_i \boldsymbol{c}_i q_i^{(1)}$$
$$= \partial_{t_1}(e_{tot}\boldsymbol{u}) + \nabla_1 \cdot (e_{tot}\boldsymbol{u}\boldsymbol{u} + (RT_0)^2 T\boldsymbol{I}) + \frac{1}{\tau_h}\boldsymbol{\sigma}^{(1)} \cdot \boldsymbol{u}$$
$$- \rho \boldsymbol{u}\boldsymbol{u} \cdot \hat{\boldsymbol{F}}^{(1)} - e_{tot}\boldsymbol{F}_{non}^{(1)}. \tag{3.29}$$

Notice that

$$\partial_{t_1}(e_{tot}\boldsymbol{u}) = \boldsymbol{u}\,\partial_{t_1} e_{tot} + e_{tot}\,\partial_{t_1}\boldsymbol{u}$$
$$= \rho\boldsymbol{u}\boldsymbol{u} \cdot \hat{\boldsymbol{F}}^{(1)} - \boldsymbol{u}\,\nabla_1 \cdot (e_{tot}\boldsymbol{u}) + e_{tot}\,\partial_{t_1}\boldsymbol{u}$$
$$= \rho\boldsymbol{u}\boldsymbol{u} \cdot \hat{\boldsymbol{F}}^{(1)} - \boldsymbol{u}\,\nabla_1 \cdot (e_{tot}\boldsymbol{u}) + e_{tot}\boldsymbol{F}_{non}^{(1)} - e_{tot}\boldsymbol{u} \cdot \nabla_1 \boldsymbol{u}$$
$$= \rho\boldsymbol{u}\boldsymbol{u} \cdot \hat{\boldsymbol{F}}^{(1)} + e_{tot}\boldsymbol{F}_{non}^{(1)} - \nabla_1 \cdot (e_{tot}\boldsymbol{u}\boldsymbol{u}). \tag{3.30}$$

Substituting this equation into (3.29) yields

$$-\frac{1}{\tau_h}\sum_i \boldsymbol{c}_i h_i^{(1)} = \nabla_1 \cdot (RT_0)^2 T\boldsymbol{I} + \frac{1}{\tau_h}\boldsymbol{\sigma}^{(1)} \cdot \boldsymbol{u}. \tag{3.31}$$

By combining the equations at both orders $O(\varepsilon)$ and $O(\varepsilon^2)$, and imposing $\lambda = (RT_0)^2\tau_h$, the following total energy transport equation is recovered:

$$\frac{\partial e_{tot}}{\partial t} + \nabla \cdot (e_{tot}\boldsymbol{u}) = \nabla \cdot \lambda\,\nabla T + \nabla \cdot (\boldsymbol{\sigma} \cdot \boldsymbol{u}) + \rho\boldsymbol{u} \cdot \hat{\boldsymbol{F}}. \tag{3.32}$$

3.5. *Lattice Boltzmann scheme*

Building on the discrete velocity kinetic models established in the previous subsections, we develop a lattice Boltzmann scheme for the non-isothermal two-phase fluid system through characteristic discretisation and trapezoidal quadrature, leading to the following implicit scheme:

$$f_i(\boldsymbol{x} + \boldsymbol{c}_i\,\delta t, t + \delta t) - f_i(\boldsymbol{x}, t) = \frac{\delta t}{2}[\Omega_f(x + \boldsymbol{c}_i\,\delta t, t + \delta t) + F_i(\boldsymbol{x} + \boldsymbol{c}_i\,\delta t, t + \delta t)]$$
$$+ \frac{\delta t}{2}[\Omega_f(x, t) + F_i(\boldsymbol{x}, t)], \tag{3.33}$$
$$h_i(\boldsymbol{x} + \boldsymbol{c}_i\,\delta t, t + \delta t) - h_i(\boldsymbol{x}, t) = \frac{\delta t}{2}[\Omega_h(x + \boldsymbol{c}_i\,\delta t, t + \delta t) + S_i(\boldsymbol{x} + \boldsymbol{c}_i\,\delta t, t + \delta t)]$$
$$+ \frac{\delta t}{2}[\Omega_h(x, t) + S_i(\boldsymbol{x}, t)], \tag{3.34}$$

where δt is the time step, $\Omega_f = (f_i^{eq} - f_i)/\tau_f$, $\Omega_h = (h_i^{eq} - h_i)/\tau_h$ and $S_i = -Z_i\tau_f\Omega_f/\tau_h + q_i$.

The implicit nature of the scheme is removed by defining the distribution functions

$$\hat{f}_i = f_i - \frac{\delta t}{2}(\Omega_f + F_i), \tag{3.35}$$
$$\hat{h}_i = h_i - \frac{\delta t}{2}(\Omega_h + S_i). \tag{3.36}$$

https://doi.org/10.1017/jfm.2026.11152 Published online by Cambridge University Press

By substituting (3.35) and (3.36) into the discrete evolution equations (3.33) and (3.34), we obtain

$$\hat{f}_i(\boldsymbol{x}+\boldsymbol{c}_i\,\delta t, t+\delta t)-\hat{f}_i(\boldsymbol{x},t)=-\omega_f[\hat{f}_i(\boldsymbol{x},t)-f_i^{eq}(\boldsymbol{x},t)]+\delta t\left(1-\frac{\omega_f}{2}\right)F_i, \quad (3.37)$$

$$\begin{aligned}
&\hat{h}_i(\boldsymbol{x}+\boldsymbol{c}_i\,\delta t, t+\delta t)-\hat{h}_i(\boldsymbol{x},t)\\
&\quad=-\omega_h\left(\hat{h}_i(\boldsymbol{x},t)-h_i^{eq}(\boldsymbol{x},t)\right)+\delta t\left(1-\frac{\omega_h}{2}\right)\left(q_i+\frac{Z_i}{\tau_h}\left(f_i-f_i^{eq}\right)\right)\\
&\quad=-\omega_h\left(\hat{h}_i(\boldsymbol{x},t)-h_i^{eq}(\boldsymbol{x},t)\right)+\delta t\left(1-\frac{\omega_h}{2}\right)q_i+\omega_h Z_i\left(1+\frac{\delta t}{2\tau_f}\right)^{-1}\left(\hat{f}_i-f_i^{eq}+\frac{\delta t}{2}F_i\right)\\
&\quad=-\omega_h\left(\hat{h}_i(\boldsymbol{x},t)-h_i^{eq}(\boldsymbol{x},t)\right)+\delta t\left(1-\frac{\omega_h}{2}\right)q_i+\omega_h\left(1-\frac{\omega_f}{2}\right)Z_i\left(\hat{f}_i-f_i^{eq}+\frac{\delta t}{2}F_i\right),
\end{aligned} \quad (3.38)$$

where $\omega_f=2\,\delta t/(2\tau_f+\delta t)$ and $\omega_h=2\,\delta t/(2\tau_h+\delta t)$. The fluid density, velocity and total energy can be computed from the new distribution function as

$$\rho=\sum_i \hat{f}_i, \quad \rho\boldsymbol{u}=\sum_i \boldsymbol{c}_i\hat{f}_i+\frac{\delta t}{2}\boldsymbol{F}_{non} \quad (3.39)$$

and

$$e_{tot}=\sum_i \hat{h}_i+\frac{\delta t}{2}\rho\boldsymbol{u}\cdot\hat{\boldsymbol{F}}. \quad (3.40)$$

In a standard lattice Boltzmann scheme, the computational domain is discretised into a uniform lattice. For example, in the D2Q9 model, the lattice spacing is set to $\delta x=c\,\delta t$, with $c=\sqrt{3RT_0}$. Consequently, the lattice size is closely dependent on the discrete velocity set, meaning that the spatial discretisation is coupled with the velocity discretisation.

3.5.1 *Boundary condition treatment*

Treating boundary conditions in the LBM requires a method to transform conditions on fluid variables into equivalent conditions for the distribution functions. This study employs dynamic boundary conditions that incorporate thermal and wetting effects. Following a boundary treatment method similar to that in Huang & Wang (2018), the boundary values for number density n, velocity $\boldsymbol{u}$ and temperature T are obtained from the dynamic boundary conditions in (2.43), (2.44) and (2.45). For a mesh point $(i,0)$ on the bottom wall, the number density at m time step $n^m(i,0)$ is calculated using a finite difference scheme

$$\begin{aligned}
n^m(i,0)=n^{m-1}(i,0)&-\frac{\delta t}{\beta}u_x^{m-1}(i,0)\left(\frac{3n^{m-1}(i,0)-4n^{m-1}(i,1)+n^{m-1}(i,2)}{2}\right)\\
&-\frac{\delta t}{\beta}L\left(n^{m-1}(i,0)\right),
\end{aligned} \quad (3.41)$$

where δt is the time step. The velocity $\mathbf{u}^m$ and temperature T^m are updated similarly. With the updated macroscopic variables on the boundary, unknown distribution functions at boundary nodes are calculated by the non-equilibrium extrapolation scheme (Guo, Zheng & Shi 2002).

In numerical simulations, it is essential to impose appropriate outflow boundary conditions at open boundaries. This study employs a constant-pressure boundary condition

https://doi.org/10.1017/jfm.2026.11152 Published online by Cambridge University Press

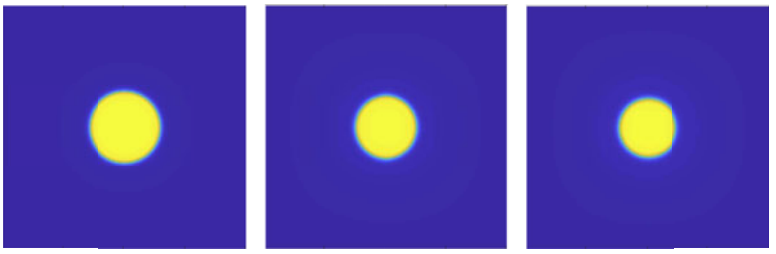


Figure 1. The density contours of droplet evaporation at different times: $t = 0.1$, $t = 0.35$, $t = 0.75$.

to model the outflow. The unknown density distribution functions are determined by the method described in Huang, Wang & Yang (2024).

4. Numerical experiments

This section presents a series of numerical experiments designed to validate the effectiveness of the proposed mesoscopic LBM. The selected benchmark cases encompass the D^2 law governing droplet evaporation, the Cox–Voinov law, droplet evaporation on heated surfaces, bubble nucleation and detachment during nucleate boiling, as well as droplet impact on a heated plate exceeding the Leidenfrost temperature.

4.1. *Validation of the scaling law*

This subsection presents a numerical study of the D^2 law for droplet evaporation and the Cox–Voinov law. We begin by examining droplet evaporation in an open environment. The process follows the D^2 law, which states that the square of the droplet diameter D decreases linearly with time, i.e.

$$\left(\frac{D}{D_0}\right)^2 = 1 - \kappa t, \tag{4.1}$$

where D_0 is the initial droplet diameter, and κ is the evaporation constant. In our simulations, the computational domain is a square with grid resolution 200×200. A droplet with initial diameter $D_0 = 60\,\delta x$ is placed at the centre of the domain. The droplet's temperature is set to the saturation temperature $T_s = 0.86T_c$, where T_c stands for the critical temperature. The surrounding vapour is maintained at a higher temperature $T_g = 1.0T_c$, while, subject to this temperature gradient at the liquid–vapour interface, the droplet undergoes evaporation.

For the temperature field, a Dirichlet condition $T = T_g$ is applied, while periodic boundary conditions are used for the velocity field. Figure 1 shows density contours at different dimensionless times, illustrating the droplet's gradual evaporation driven by the interfacial temperature gradient. Quantitatively, figure 2 plots the temporal evolution of the squared droplet diameter, showing excellent agreement with the D^2 law.

Next, we consider a droplet deposited on a smooth substrate with initial contact angle $\theta_0 > \theta_{eq}$, which spreads and relaxes towards an equilibrium shape determined by θ_{eq}. The spreading dynamics can be quantitatively analysed using the Cox–Voinov law, which relates the apparent contact angle θ_a to the velocity U of the moving contact line via

$$\theta_a^3 - \theta_{eq}^3 \propto Ca, \tag{4.2}$$

where the capillary number is defined as $Ca = \mu U/\gamma$. Here, μ is the dynamic viscosity, and γ is the surface tension. We set $\mu = 0.167$ N s m^{-2} in our simulations.

https://doi.org/10.1017/jfm.2026.11152 Published online by Cambridge University Press

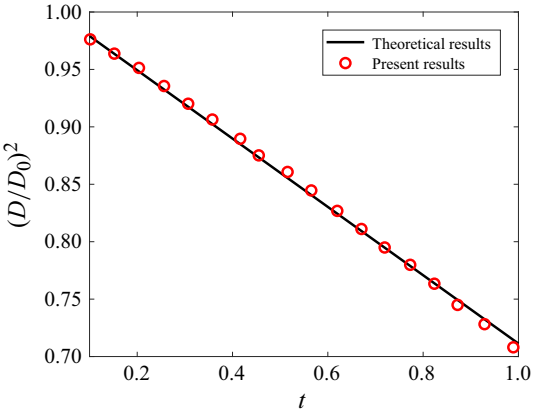


Figure 2. Time evolution of the square of the dimensionless diameter for the present model.

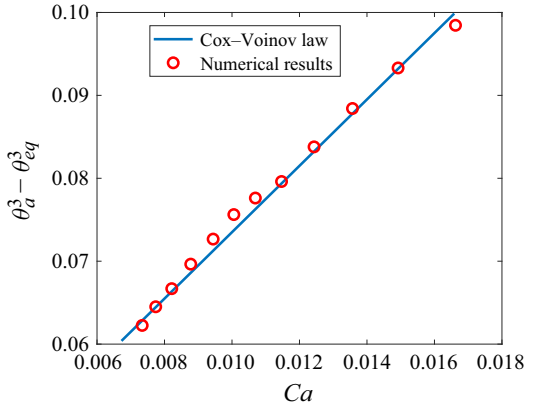


Figure 3. Numerical validation of the Cox–Voinov law.

The simulations are conducted on a $256 \times 256 \times 256$ lattice. Initially, a droplet with contact angle $\theta_0 = 2/3\pi$ is placed at the centre of the substrate, and the equilibrium contact angle is taken as $\theta_{eq} = \pi/3$. To extract the dynamic contact angle from the simulation data, we assume that the droplet is closely approximated by a spherical-cap shape after an initial transition period. Under this assumption and by enforcing volume conservation, the contact angle can be determined numerically. The volume V of a spherical cap is given by

$$V = \frac{\pi}{3} R^3 (2 + \cos\theta_a)(1 - \cos\theta_a)^2. \tag{4.3}$$

Since our numerical scheme conserves mass, the droplet volume V remains constant. By measuring the droplet height $h_d(t)$ and contact line diameter $2\,r(t)$, we compute the time-dependent radius of the droplet as

$$R(t) = \frac{r(t)^2 + h_d(t)^2}{2\,h_d(t)}, \tag{4.4}$$

then solve (4.3) for the contact angle $\theta(t)$. Figure 3 shows a plot of $\theta^3(t) - \theta_{eq}^3$ versus Ca from a numerical simulation of a spreading droplet. The linear scaling observed confirms excellent agreement with the Cox–Voinov law.

https://doi.org/10.1017/jfm.2026.11152 Published online by Cambridge University Press

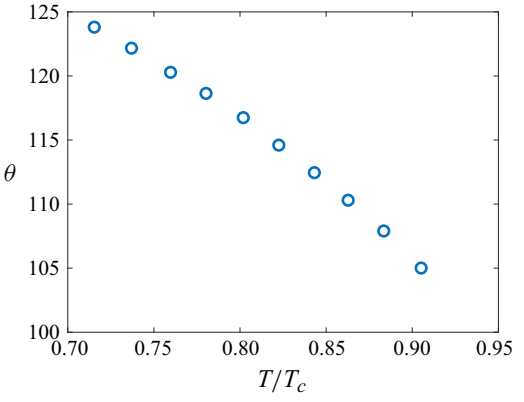


Figure 4. Dependence of the apparent contact angle on wall temperature.

In addition, we also investigated the effect of wall temperature on the apparent contact angle θ. The numerical results are illustrated in figure 4. It can be observed that the apparent contact angle gradually decreases with increasing wall temperature, which is consistent with theoretical predictions (Adamson 1973; Sullivan 1981; Diaz *et al.* 2017).

4.2. *Leidenfrost droplet impact on a flat plate*

Droplet impact on a heated plate above the Leidenfrost temperature is a phenomenon that has attracted considerable research interest. In this subsection, the developed model and LBM are validated through simulations of a droplet impacting a heated plate above the Leidenfrost temperature. The initial droplet radius is set as $R_0 = 50$. The liquid and vapour saturation temperature, denoted as T_s, is maintained at $0.8T_c$, leading to the corresponding coexistence densities $\rho_l = 7.2$ and $\rho_g = 0.197$. Under these conditions, the measured surface tension γ is determined to be 0.11235.

To facilitate a more precise comparison with experimental data, several dimensionless numbers are introduced to align with realistic conditions. The Prandtl number for the liquid phase is defined as

$$Pr_l = \frac{\mu_l c_{vl}}{\lambda_l}, \tag{4.5}$$

while the Prandtl number for the gas phase is given by

$$Pr_g = \frac{\mu_g c_{vg}}{\lambda_g}, \tag{4.6}$$

where μ_l, μ_g, c_{vl}, c_{vg}, λ_l and λ_g are the dynamic viscosities, the specific heat capacities, and the thermal conductivities of the liquid phase and the gas phase, respectively. Additionally, the Jakob number is incorporated as

$$Ja = \frac{c_{vl}(T_w - T_s)}{h_{fg}}, \tag{4.7}$$

where T_w is the wall temperature, and h_{fg} is the latent heat, which is calculated by $h_{fg} = h_g - h_l$, with h_g and h_l the enthalpy values of the gas and liquid phases, respectively. The Weber number and Bond number are also considered to represent the experimental

https://doi.org/10.1017/jfm.2026.11152 Published online by Cambridge University Press

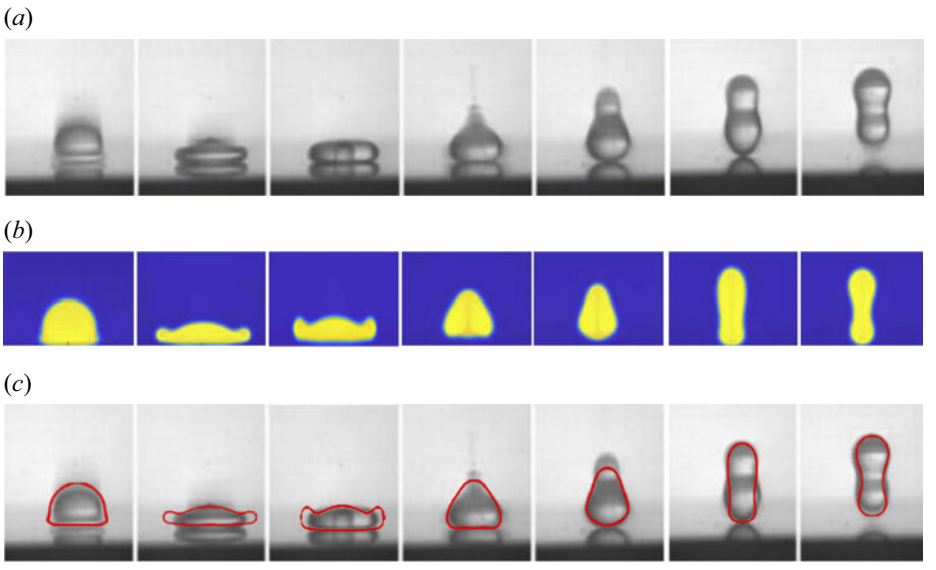


Figure 5. The experiment snapshots and simulation results for droplet impact on a heated plate.

conditions, given by

$$We = \frac{D_0 \rho_l U^2}{\gamma}, \quad Bo = \frac{\rho_l g D_0^2}{\gamma}, \tag{4.8}$$

where U is the droplet initial velocity. In our simulations, the selected parameters are $c_{vl} = 7.4$, $c_{vg} = 3.4$, $\lambda_l = 0.25$ and $\lambda_g = 0.1$, which result in Prandtl numbers $Pr_g = 0.94$ and $Pr_l = 1.49$, respectively.

For the boundary conditions, the top of the domain is defined as an outflow boundary, while the bottom solid wall is treated as a no-slip boundary maintained at a constant temperature T_w. Periodic conditions are applied to the lateral boundaries. Given that the contact temperature between the droplet and the heated plate rapidly equilibrates to T_w upon impact, the temperature of the adjacent fluid layer is also set to T_w.

The proposed model is validated against the experimental study in Biance *et al.* (2006), where a water droplet with initial radius $R_0 = 1$ mm impacts a flat plate heated to 300 °C at initial velocity 0.8 m s^{-1}. The corresponding dimensionless parameters in this case are set to be $Ja = 0.50$, $We = 21.6$, $Bo = 0.16$.

A comparison of the simulation results with experimental snapshots is presented in figure 5. The numerical results show excellent agreement with experimental observations, confirming that the developed lattice Boltzmann model reliably predicts Leidenfrost droplet impingement dynamics.

For a more quantitative validation, we further examine the experimental study by Wachters *et al.* (1966), where the dimensionless numbers are specified as $We = 16$ and $Ja = 0.61$. The evolution of the droplet's gravitational centre height, denoted as ϵ_{mass}, is computed and compared with the corresponding experimental data. The gravitational centre height of the droplet is determined using the expression

$$\epsilon_{mass} = \frac{\sum_{\rho > \rho_{avg}} \rho(\boldsymbol{x})\, h(\boldsymbol{x})}{\sum_{\rho > \rho_{avg}} \rho(\boldsymbol{x})}, \tag{4.9}$$

https://doi.org/10.1017/jfm.2026.11152 Published online by Cambridge University Press

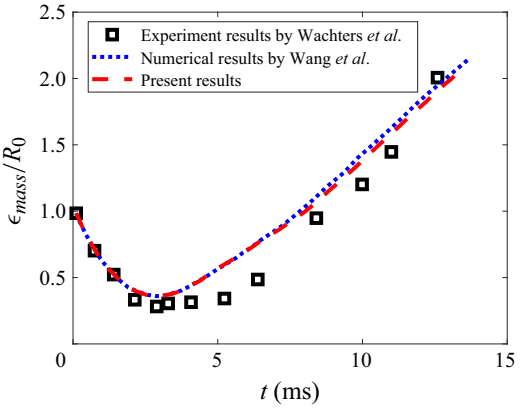


Figure 6. Comparison of the evolution of the height of the dimensionless droplet gravity centre at $We = 16$, $Ja = 0.61$.

where $h(\boldsymbol{x})$ denotes the height of each computational cell, and $\rho(\boldsymbol{x})$ represents the local density within the cell.

The numerical results obtained from the present model, along with the experimental data reported by Wachters *et al.* (1966), are depicted in figure 6. As illustrated in the figure, the simulation results exhibit strong agreement with both the experimental data and the numerical results in Wang *et al.* (2022*a*), further validating the accuracy and reliability of the proposed model in capturing the Leidenfrost droplet dynamics.

4.3. *Droplet evaporation on a heated surface*

The evaporation of droplets on heated surfaces represents a fundamental heat transfer process that is prevalent across numerous engineering applications. In this subsection, we aim to investigate the phenomenon of droplet evaporation on a heated surface, and validate the numerical results through comparison with the experimental data reported in Dash & Garimella (2014). Within the numerical framework, the Jakob number is employed to characterise the ratio of sensible heat to latent heat during the phase transition between liquid and vapour.

In the present numerical simulation, a three-dimensional computational domain with grid resolution $200 \times 200 \times 200$ is employed. Initially, a droplet with diameter 70 lattice units is positioned at the centre of the heated wall, with its temperature specified as $T_s = 0.86T_c$. Periodic boundary conditions are imposed in the x- and y-directions, whereas a constant-pressure boundary condition is applied at the top boundary. Furthermore, the temperatures of the bottom and top boundaries are maintained at T_w and T_s, respectively, throughout the simulations. Under the condition $c_{vl} = 5.0$, the wall temperature is set to $T_w = 0.8931T_c$.

Figure 7 shows the evolution of the droplet profile at different times, as predicted by the proposed model, alongside corresponding experimental results from Dash & Garimella (2014) for validation. The droplet gradually evaporates due to the vapour pressure difference between the liquid–vapour interface and the outlet. Furthermore, comparison with the experimental data confirms that the present model accurately captures the morphological evolution of the evaporating droplet.

Figure 8 shows the temporal evolution of the droplet radius from the present three-dimensional numerical model, with experimental data and numerical results from Huang *et al.* (2024) also shown for comparison. In this figure, the droplet radius and time are

https://doi.org/10.1017/jfm.2026.11152 Published online by Cambridge University Press

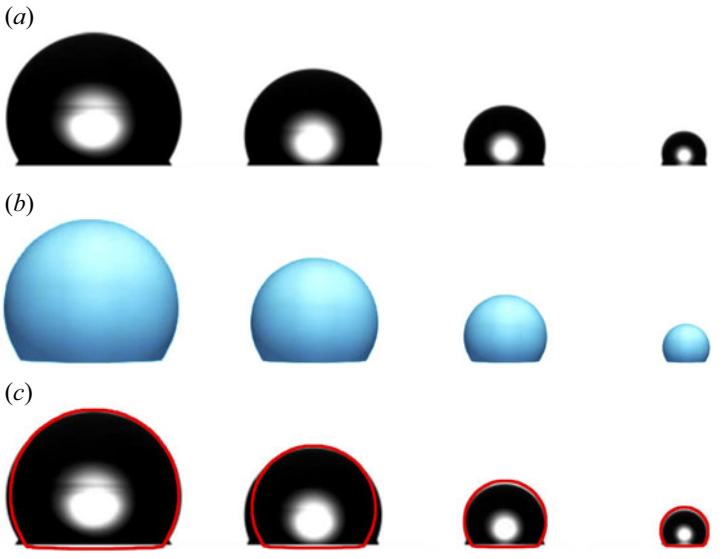


Figure 7. Comparison of the experiment snapshots and simulation results of droplet evaporation on a heated surface: three-dimensional simulation.

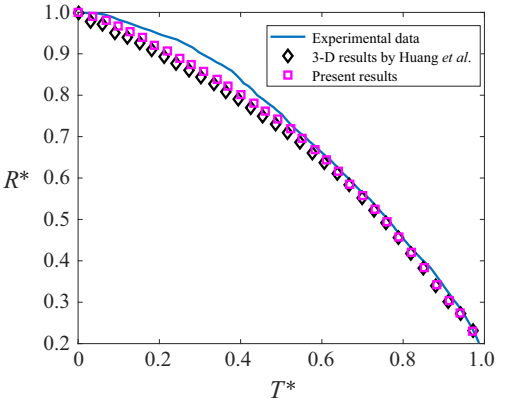


Figure 8. Profiles of the normalised radius R^* with the dimensionless time T^*.

normalised using a reference case with droplet diameter 20 lattice units. The results from our three-dimensional simulations are in excellent agreement with both the experimental measurements and the prior numerical data.

4.4. *Bubble nucleation and departure*

To further evaluate the performance of the proposed model and numerical algorithm, we conduct simulations for the liquid–vapour phase change process, specifically examining bubble nucleation and departure in nucleate boiling. The computational domain is discretised with mesh resolution $100 \times 100 \times 150$. Initially, the cavity is entirely filled with saturated liquid, and the system's temperature is maintained at $T_s = 0.86T_c$. A localised heating region, represented by a square area of 4 lattice units in length at the bottom centre, is maintained at fixed temperature $T_w = 0.96T_c$, while the remaining walls are held at the saturated temperature $T_s = 0.86T_c$.

https://doi.org/10.1017/jfm.2026.11152 Published online by Cambridge University Press

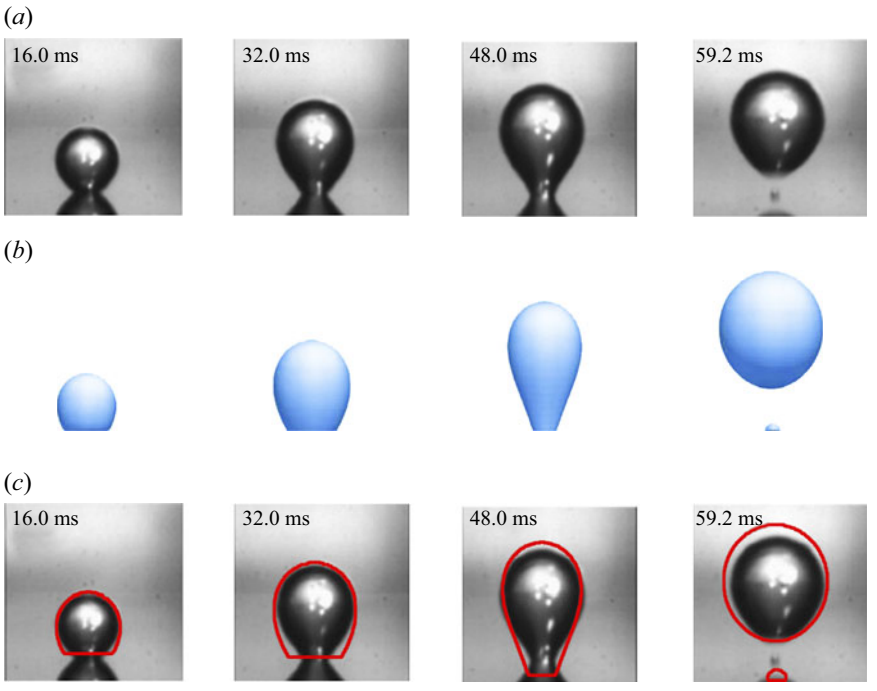


Figure 9. Distributions of the density contours in nucleate boiling and the comparison with experimental.

The equilibrium contact angle is prescribed as 100°. A no-slip boundary condition is enforced at the solid walls, whereas periodic boundary conditions are applied along the x- and y-directions. The fluid properties, including the specific heat at constant volume, remain consistent with those used in the previous subsection, and the thermal conductivity is set to $2/3$. Furthermore, a buoyant force, defined as $\boldsymbol{F}_b = (\rho - \rho_{ave})\boldsymbol{g}$, is incorporated into the velocity field, where ρ_{ave} denotes the average density over the entire system, and $\boldsymbol{g}$ represents the gravitational acceleration.

Figure 9 depicts the evolution of bubble morphology as predicted by the present thermal lattice Boltzmann model, alongside experimental observations reported in Mukherjee & Dhir (2004). The numerical results effectively capture the key stages of bubble nucleation, growth and departure, demonstrating strong agreement with experimental findings in terms of bubble dynamics and growth patterns.

To further quantify the numerical predictions, the power-law relationship between the bubble departure diameter and gravitational acceleration is examined. Figure 10 presents the variation of the bubble departure diameter D_d as a function of gravity acceleration, where the solid line represents the theoretical relationship $D_d = 0.166g^{-0.5}$. The comparison reveals that the departure diameters predicted by different numerical models are in close agreement, and the observed dependency of D_d on $g^{-0.5}$ aligns well with the theoretical results proposed in Dhir (2006). These findings further validate the effectiveness of the present model and the lattice Boltzmann scheme in simulating liquid–vapour phase change phenomena.

Finally, it is worth noting that the phase transition in our deterministic model is induced by the spinodal instability of the free energy. In fact, the nucleation threshold for superheating given by the deterministic models is larger than observed in experiments. The genuine nucleation of a vapour bubble in a liquid is induced by thermal stochastic fluctuations (Lohse & Prosperetti 2016; Menzl *et al.* 2016). Recently, nucleation in

https://doi.org/10.1017/jfm.2026.11152 Published online by Cambridge University Press

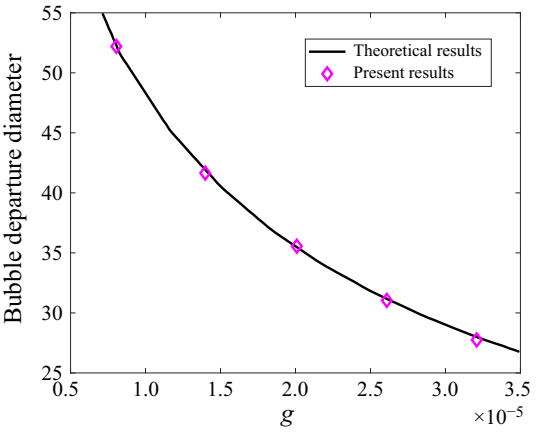


Figure 10. Variation of bubble departure diameter with gravity acceleration.

liquid–vapour phase transitions has been studied using a fluctuation hydrodynamic theory (Gallo *et al.* 2020, 2021, 2023). In these studies, the stochastic model demonstrates excellent agreement with experimental data regarding the onset temperature, and provides a promising approach for accurately predicting nucleation phenomena.

5. Conclusions

In conclusion, we propose a novel unified variational framework for deriving thermodynamically consistent models of non-isothermal, one-component multiphase flows involving liquid–vapour phase transitions and wetting effects. This framework extends the applicability of the Onsager variational principle – traditionally used for overdamped systems – to incorporate both inertial and thermal effects. Its adaptability suggests broad applicability to other complex systems, such as multicomponent and multiphase flows. To efficiently solve the resulting system of equations, we also develop a lattice Boltzmann method (LBM). A key innovation of our LBM is the use of an additional distribution function representing total energy, distinct from the internal energy or temperature representations employed in prior studies. Numerical experiments demonstrate good agreement between the present LBM results and existing theoretical and numerical benchmarks. Furthermore, the model successfully captures complex phenomena, including evaporation, condensation, pool boiling and droplet/bubble dynamics within non-uniform thermal fields. While the current numerical simulations primarily utilise the van der Waals equation of state, future work will investigate multicomponent and multiphase flows governed by other equations of state, such as the Peng–Robinson model.

Funding. This work is partially supported by the National Key R&D Programme of China (no. 2024YFA1012502) and by the CAS AMSS-PolyU Joint Laboratory of Applied Mathematics (no. JLFS/P-501/24). The work of Z.Q. is partially supported by the Hong Kong Research Grants Council RFS grant RFS2021-5S03, GRF grant 15305624 and NSFC/RGC Joint Research Scheme grant N_PolyU5145/24. The work of X.X. is partially supported by the National Natural Science Foundation of China (nos 12371415 and 12461160275) and the Beijing Natural Science Foundation (no. Z240001). The work of X.Y. is partially supported by the National Natural Science Foundation of China (grant no. 12372286), the science and technology innovation programme of Hunan Province, China (grant no. 2024RC3228) and the Excellent Youth Foundation of Changsha Scientific Committee, China (grant no. kq2306023). The work of Y.Z. is partially supported by the National Natural Science Foundation of China (no. 12301554) and the Natural Science Foundation of Jiangsu Province (no. BK20220368).

https://doi.org/10.1017/jfm.2026.11152 Published online by Cambridge University Press

Declaration of interests. The authors report no conflict of interest.

Declaration of generative AI and AI-assisted technologies in the writing process. During the preparation of this work, the authors used DeepSeek in order to improve the English writing and readability of some part of the paper. After using this tool/service, the authors reviewed and edited the content as needed, and take full responsibility for the content of the published article.

References

ADAMSON, A.W. 1973 Potential distortion model for contact angle and spreading. II. Temperature dependence effects. *J. Colloid Interface Sci.* **44**, 273.

AIDUN, C.K. & CLAUSEN, J.R. 2010 Lattice Boltzmann method for complex flows. *Annu. Rev. Fluid Mech.* **42**, 439–472.

ANDERSON, D.M., MCFADDEN, G.B. & WHEELER, A.A. 1998 Diffuse-interface methods in fluid mechanics. *Annu. Rev. Fluid Mech.* **30** (1), 139–165.

BIANCE, A.L., CHEVY, F., CLANET, C., LAGUBEAU, G. & QUÉRÉ, D. 2006 On the elasticity of an inertial liquid shock. *J. Fluid Mech.* **554**, 47–66.

BOUILLANT, A., MOUTERDE, T., BOURRIANNE, P., LAGARDE, A., CLANET, C. & QUÉRÉ, D. 2018 Leidenfrost wheels. *Nat. Phys.* **14** (12), 1188–1192.

CHEN, S. & DOOLEN, G. 1998 Lattice Boltzmann method for fluid flows. *Annu. Rev. Fluid Mech.* **30**, 329–364.

CHENG, P., QUAN, X., GONG, S., LIU, X. & YANG, L. 2014 Recent analytical and numerical studies on phase-change heat transfer. *Adv. Heat Transfer* **46**, 187–248.

CIRA, N.J., BENUSIGLIO, A. & PRAKASH, M. 2015 Vapour-mediated sensing and motility in two-component droplets. *Nature* **519** (7544), 446–450.

DASH, S. & GARIMELLA, S.V. 2014 Droplet evaporation on heated hydrophobic and superhydrophobic surfaces. *Phys. Rev. E* **89** (4), 042402.

DHIR, V.K. 1998 Boiling heat transfer. *Annu. Rev. Fluid Mech.* **30**, 365–401.

DHIR, V.K.2006 Mechanistic prediction of nucleate boiling heat transfer – achievable or a hopeless task? *J. Heat Transfer* **128** (1), 1–12.

DIAZ, M.E., SAVAGE, M.D. & CERRO, R.L. 2017 The effect of temperature on contact angles and wetting transitions for *n*-alkanes on PTFE. *J. Colloid Interface Sci.* **503**, 159.

DOI, M. 2011 Onsager's variational principle in soft matter. *J. Phys.: Condens. Matter* **23**, 284118.

DOI, M. 2013 *Soft Matter Physics*. Oxford University Press.

GALLO, M., MAGALETTI, F. & CASCIOLA, C.M. 2021 Heterogeneous bubble nucleation dynamics. *J. Fluid Mech.* **906**, A20.

GALLO, M., MAGALETTI, F., COCCO, D. & CASCIOLA, C.M. 2020 Nucleation and growth dynamics of vapour bubbles. *J. Fluid Mech.* **883**, A14.

GALLO, M., MAGALETTI, F., GEORGOULAS, A., MARENGO, M., DE CONINCK, J. & CASCIOLA, C.M. 2023 A nanoscale view of the origin of boiling and its dynamics. *Nat. Commun.* **14** (1), 6428.

GONG, S. & CHENG, P. 2012 A lattice Boltzmann method for simulation of liquid–vapor phase-change heat transfer. *Intl J. Heat Mass Transfer* **55** (17–18), 4923–4927.

GRAEBER, G., REGULAGADDA, K., HODEL, P., KÜTTEL, C., LANDOLF, D., SCHUTZIUS, T.M. & POULIKAKOS, D. 2021 Leidenfrost droplet trampolining. *Nat. Commun.* **12** (1), 1727.

GUAN, D., WANG, Y., CHARLAIX, E. & TONG, P. 2016 Asymmetric and speed-dependent capillary force hysteresis and relaxation of a suddenly stopped moving contact line. *Phys. Rev. Lett.* **116** (6), 066102.

GUO, Z. & SHU, C. 2013 *Lattice Boltzmann Method and Its Applications in Engineering*. World Scientific.

GUO, Z. & LIN, P. 2015 A thermodynamically consistent phase-field model for two-phase flows with thermocapillary effects. *J. Fluid Mech.* **766**, 226–271.

GUO, Z., ZHENG, C.G. & SHI, B.C. 2002 An extrapolation method for boundary conditions in lattice Boltzmann method. *Phys. Fluids* **14** (6), 2007–2010.

GUO, Z., ZHENG, C.G., SHI, B.C. & ZHAO, T.S. 2007 Thermal lattice Boltzmann equation for low Mach number flows: decoupling model. *Phys. Rev. E* **75** (3), 036704.

GUO, Z. 2021 Well-balanced lattice Boltzmann model for two-phase systems. *Phys. Fluids* **33** (3), 031709.

HE, Y.L., LIU, Q. & LI, Q. 2019 Lattice Boltzmann methods for single-phase and solid–liquid phase-change heat transfer in porous media: a review. *Intl J. Heat Mass Transfer* **129**, 160–197.

HODES, M., KANE, D., BAZANT, M.Z. & KIRK, T.L. 2023 Asymptotic Nusselt numbers for internal flow in the Cassie state. *J. Fluid Mech.* **977**, A18.

HOHENBERG, P.C. & HALPERIN, B.I. 1977 Theory of dynamic critical phenomena. *Rev. Mod. Phys.* **49** (3), 435–479.

https://doi.org/10.1017/jfm.2026.11152 Published online by Cambridge University Press

HUANG, H., SUKOP, M.C. & LU, X.Y. 2015 *Multiphase Lattice Boltzmann Methods: Theory and Application*. John Wiley & Sons.
HUANG, J., WANG, L. & YANG, X. 2024 An efficient thermal lattice Boltzmann method for simulating three-dimensional liquid–vapor phase change. *Comput. Fluids* **273**, 106214.
HUANG, J. & WANG, X. 2018 A lattice Boltzmann model for multiphase flows with moving contact line and variable density. *J. Comput. Phys.* **353**, 26–45.
HUANG, R., WU, H. & ADAMS, N.A. 2021 Mesoscopic lattice Boltzmann modeling of the liquid–vapor phase transition. *Phys. Rev. Lett.* **126** (24), 244501.
HUH, C. & SCRIVEN, L.E. 1971 Hydrodynamic model of steady movement of a solid/liquid/fluid contact line. *J. Colloid Interface Sci.* **35** (1), 85–101.
HYON, Y., KWAK, D.Y. & LIU, C. 2010 Energetic variational approach in complex fluids: maximum dissipation principle. *Discrete Contin. Dyn. Syst.* **26** (4), 1291–1304.
JACQMIN, D. 2000 Contact-line dynamics of a diffuse fluid interface. *J. Fluid Mech.* **402**, 57–88.
KAVURI, S., KARAPETSAS, G., SHARMA, C.S. & SAHU, K.C. 2025 Evaporation-driven coalescence of two droplets undergoing freezing. *J. Fluid Mech.* **1006**, A21.
KOU, J. & SUN, S. 2018*a* Thermodynamically consistent modeling and simulation of multi-component two-phase flow with partial miscibility. *Comput. Meth. Appl. Mech. Engng* **331**, 623–649.
KOU, J. & SUN, S. 2018*b* Thermodynamically consistent simulation of nonisothermal diffuse-interface two-phase flow with Peng–Robinson equation of state. *J. Comput. Phys.* **371**, 581–605.
LACIS, U., JOHANSSON, P., FULLANA, T., HESS, B., AMBERG, G., BAGHERI, S. & ZALESKI, S. 2020 Steady moving contact line of water over a no-slip substrate: challenges in benchmarking phase-field and volume-of-fluid methods against molecular dynamics simulations. *Eur. Phys. J. Special Topics* **229**, 1897–1921.
LACIS, U., PELLEGRINO, M., SUNDIN, J., AMBERG, G., ZALESKI, S., HESS, B. & BAGHERI, S. 2022 Nanoscale sheared droplet: volume-of-fluid, phase-field and no-slip molecular dynamics. *J. Fluid Mech.* **940**, A10.
LI, Q., LUO, K.H. & KANG, Q.J. 2016 Lattice Boltzmann methods for multiphase flow and phase-change heat transfer. *Prog. Energy Combust. Sci.* **52**, 62–105.
LIU, C., QIAN, T. & XU, X. 2012 Hydrodynamic boundary conditions for one-component liquid–gas flows on non-isothermal solid substrates. *Commun. Math. Sci.* **10** (4), 1027–1053.
LOHSE, D. & PROSPERETTI, A. 2016 Homogeneous nucleation: patching the way from the macroscopic to the nanoscopic description. *Proc. Natl Acad. Sci. USA* **113** (48), 13549–13550.
LOPEZ-ECHEVERRY, J.S., REIF-ACHERMAN, S. & ARAUJO-LOPEZ, E. 2017 Peng–Robinson equation of state: 40 years through cubics. *Fluid Phase Equilib.* **447**, 39–71.
MAGALETTI, F., GALLO, M., MARINO, L. & CASCIOLA, C.M. 2016 Shock-induced collapse of a vapor nanobubble near solid boundaries. *Intl J. Multiphase Flow* **84**, 34–45.
MAGALETTI, F., GALLO, M., PEREZ, S.P., CARRILLO, J.A. & KALLIADASIS, S. 2022 A positivity-preserving scheme for fluctuating hydrodynamics. *J. Comput. Phys.* **463**, 111248.
MAN, X. & DOI, M. 2017 Vapor-induced motion of liquid droplets on an inert substrate. *Phys. Rev. Lett.* **119** (4), 044502.
MAYER, M.D., KIRK, T.L., HODES, M. & CROWDY, D. 2025 Mechanical power from thermocapillarity on superhydrophobic surfaces. *J. Fluid Mech.* **1009**, A33.
MENZL, G., GONZALEZ, M.A., GEIGER, P., CAUPIN, F., ABASCAL, J.L.F., VALERIANI, C. & DELLAGO, C. 2016 Molecular mechanism for cavitation in water under tension. *Proc. Natl Acad. Sci. USA* **113** (48), 13582–13587.
MUKHERJEE, A. & DHIR, V.K. 2004 Study of lateral merger of vapor bubbles during nucleate pool boiling. *J. Heat Transfer* **126** (6), 1023–1039.
ONSAGER, L. 1931*a* Reciprocal relations in irreversible processes. I. *Phys. Rev.* **37** (4), 405–426.
ONSAGER, L. 1931*b* Reciprocal relations in irreversible processes. II. *Phys. Rev.* **38** (12), 2265–2279.
ONUKI, A. 2002 *Phase Transition Dynamics*. Cambridge University Press.
ONUKI, A. 2005 Dynamic van der Waals theory of two-phase fluids in heat flow. *Phys. Rev. Lett.* **94** (5), 054501.
ONUKI, A. 2007 Dynamic van der Waals theory. *Phys. Rev. E* **75** (3), 036304.
ÖTTINGER, H.C. 2005 *Beyond Equilibrium Thermodynamics*. Wiley-interscience.
PENG, D.-Y. & ROBINSON, D.B. 1976 A new two-constant equation of state. *Ind. Engng Chem. Fundam.* **15** (1), 59–64.
QIAN, T., WANG, X.-P. & SHENG, P. 2003 Molecular scale contact line hydrodynamics of immiscible flows. *Phys. Rev. E* **68** (1), 016306.

https://doi.org/10.1017/jfm.2026.11152 Published online by Cambridge University Press

QIAN, T., WANG, X.-P. & SHENG, P. 2006 A variational approach to moving contact line hydrodynamics. *J. Fluid Mech.* **564**, 333–360.

QIAO, Z.H., YANG, X.G. & ZHANG, Y.Z. 2019 Thermodynamic-consistent multiple relaxation-time lattice Boltzmann equation model for two-phase hydrocarbon fluids with Peng–Robinson equation of state. *Intl J. Heat Mass Transfer* **141**, 1216–1226.

QIAO, Z.H., YANG, X.G. & ZHANG, Y.Z. 2021 A novel lattice Boltzmann model for fourth order nonlinear partial differential equations. *J. Sci. Comput.* **87** (1), 1–18.

QIAO, Z.H., YANG, X.G. & ZHANG, Y.Z. 2024 A free-energy based multiple-distribution function lattice Boltzmann method for multi-component and multi-phase flows. *Appl. Therm. Engng* **257**, 124241.

QUÉRÉ, D. 2013 Leidenfrost dynamics. *Annu. Rev. Fluid Mech.* **45** (1), 197–215.

REN, W. 2007 Boundary conditions for the moving contact line problem. *Phys. Fluids* **19** (2), 022101.

REN, W. & E, W. 2011 Derivation of continuum models for the moving contact line problem based on thermodynamic principles. *Commun. Math. Sci.* **9** (2), 597–606.

SCHWEIGLER, K.M., SAID, M.B., SEIFRITZ, S., SELZER, M. & NESTLER, B. 2017 Experimental and numerical investigation of drop evaporation depending on the shape of the liquid/gas interface. *Intl J. Heat Mass Transfer* **105**, 655–663.

SHIKHMURZAEV, Y.D. 2007 *Capillary Flows with Forming Interfaces*. Chapman and Hall/CRC.

SMEJKAL, T. & MIKY, J. 2017 Phase stability testing and phase equilibrium calculation at specified internal energy, volume, and moles. *Fluid Phase Equilib.* **431**, 82–96.

SNOEIJER, J.H. & ANDREOTTI, B. 2013 Moving contact lines: scales, regimes, and dynamical transitions. *Annu. Rev. Fluid Mech.* **45** (1), 269–292.

SUI, Y., DING, H. & SPELT, P.D.M. 2014 Numerical simulations of flows with moving contact lines. *Annu. Rev. Fluid Mech.* **46** (1), 97–119.

SULLIVAN, D.E. 1981 Surface tension and contact angle of a liquid–solid interface. *J. Chem. Phys.* **74**, 2604.

SUN, Y., WU, J., JIANG, M., WISE, S.M. & GUO, Z. 2024 A thermodynamically consistent phase-field model and an entropy stable numerical method for simulating two-phase flows with thermocapillary effects. *Appl. Numer. Math.* **206**, 161–189.

TANG, Q., ZHONG, L., TANG, C. & HUANG, Y. 2024 Unified theoretical framework for temperature regulation via phase transition. *Phys. Rev. E* **110** (1), 014112.

TOMAR, G., BISWAS, G., SHARMA, A. & AGRAWAL, A. 2005 Numerical simulation of bubble growth in film boiling using a coupled level-set and volume-of-fluid method. *Phys. Fluids* **17** (11), 112103.

WACHTERS, L.H.J., SMULDERS, L., VERMEULEN, J.R. & KLEIWEG, H.C. 1966 The heat transfer from a hot wall to impinging mist droplets in the spheroidal state. *Chem. Engng Sci.* **21** (12), 1231–1248.

WALDMANN, L. 1967 Non-equilibrium thermodynamics of boundary conditions. *Z. Naturforsch. A* **22** (8), 1269–1280.

WANG, G., FEI, L., LEI, T., WANG, Q. & LUO, K.H. 2022*a* Droplet impact on a heated porous plate above the Leidenfrost temperature: a lattice Boltzmann study. *Phys. Fluids* **34** (9), 093319.

WANG, L., HUANG, J.X. & HE, K. 2022*b* A new thermal lattice Boltzmann model for liquid vapor phase change. *Phys. Rev. E* **106** (5), 055308.

WANG, Q. 2021 Generalized Onsager principle and its applications. In *Frontiers and Progress of Current Soft Matter Research* (ed. X.Y. Liu), pp. 101–132. Springer.

WANG, Y.W. & LIU, C. 2022 Some recent advances in energetic variational approaches. *Entropy* **24** (5), 721.

WELCH, S.W.J. & WILSON, J. 2000 A volume of fluid-based method for fluid flows with phase change. *J. Comput. Phys.* **160** (2), 662–682.

WILSON, S.K. & D'AMBROSIO, H.-M. 2023 Evaporation of sessile droplets. *Annu. Rev. Fluid Mech.* **55** (1), 481–509.

XU, X. 2023 A variational analysis for the moving finite element method for gradient flows. *J. Comput. Math.* **41** (2), 191–210.

XU, X., DI, Y. & DOI, M. 2016 Variational method for contact line problems in sliding liquids. *Phys. Fluids* **28** (8), 087101.

XU, X. & QIAN, T. 2012 Thermal singularity and droplet motion in one-component fluids on solid substrates with thermal gradients. *Phys. Rev. E* **85** (6), 061603.

XU, X. & QIAN, T. 2013 Hydrodynamics of Leidenfrost droplets in one-component fluids. *Phys. Rev. E* **87** (4), 043013.

XU, X. & QIAN, T. 2014 Single-bubble dynamics in pool boiling of one-component fluids. *Phys. Rev. E* **89** (6), 063002.

ZHAKHOVSKY, V.V., KRYUKOV, A.P., LEVASHOV, V.Y., SHISHKOVA, I.N. & ANISIMOV, S.I. 2019 Mass and heat transfer between evaporation and condensation surfaces: atomistic simulation and solution of Boltzmann kinetic equation. *Proc. Natl Acad. Sci. USA* **116** (37), 18209–18217.

https://doi.org/10.1017/jfm.2026.11152 Published online by Cambridge University Press

ZHANG, W.H., KUANG, S.B., CHAI, Z.H. & SHI, B.C. 2025 Thirteen-velocity three-dimensional multiple-relaxation-time lattice Boltzmann model for incompressible Navier–Stokes equations. *Adv. Appl. Math. Mech.* **17** (4), 1037–1062.

ZHANG, Z. & XU, X. 2022 Effective boundary conditions for dynamic contact angle hysteresis on chemically inhomogeneous surfaces. *J. Fluid Mech.* **935**, A34.

https://doi.org/10.1017/jfm.2026.11152 Published online by Cambridge University Press